energies

MDPI

Review

A Review on Recent Progress in the Integrated Green Hydrogen Production Processes

Mohsen Fallah Vostakola [1], Babak Salamatinia [2] and Bahman Amini Horri [3,*]

[1] School of Metallurgy and Materials Engineering, Iran University of Science and Technology (IUST), Narmak, Tehran 16846-13114, Iran; mohsenfallahvostakola@gmail.com
[2] Discipline of Chemical Engineering, School of Engineering, Monash University Malaysia, Jalan Lagoon Selatan, Bandar Sunway, Subang Jaya 47500, Selangor, Malaysia; babak.salamatinia@monash.edu
[3] Department of Chemical and Process Engineering, University of Surrey, Surrey GU2 7XH, UK
* Correspondence: b.aminihorri@surrey.ac.uk; Tel.: +44-(0)-1483-689846

Abstract: The thermochemical water-splitting method is a promising technology for efficiently converting renewable thermal energy sources into green hydrogen. This technique is primarily based on recirculating an active material, capable of experiencing multiple reduction-oxidation (redox) steps through an integrated cycle to convert water into separate streams of hydrogen and oxygen. The thermochemical cycles are divided into two main categories according to their operating temperatures, namely low-temperature cycles (<1100 °C) and high-temperature cycles (<1100 °C). The copper chlorine cycle offers relatively higher efficiency and lower costs for hydrogen production among the low-temperature processes. In contrast, the zinc oxide and ferrite cycles show great potential for developing large-scale high-temperature cycles. Although, several challenges, such as energy storage capacity, durability, cost-effectiveness, etc., should be addressed before scaling up these technologies into commercial plants for hydrogen production. This review critically examines various aspects of the most promising thermochemical water-splitting cycles, with a particular focus on their capabilities to produce green hydrogen with high performance, redox pairs stability, and the technology maturity and readiness for commercial use.

Keywords: thermochemical water splitting; green hydrogen production; redox loop; high-temperature cycles; low-temperature cycles; large-scale hydrogen production

Citation: Fallah Vostakola, M.; Salamatinia, B.; Amini Horri, B. A Review on Recent Progress in the Integrated Green Hydrogen Production Processes. *Energies* **2022**, *15*, 1209. https://doi.org/10.3390/en15031209

Academic Editor: Muhammad Aziz

Received: 4 January 2022
Accepted: 4 February 2022
Published: 7 February 2022

1. Introduction

The ever-growing energy demand and its associated greenhouse gas emissions are two of the most challenging issues which need to be addressed in the near future. Currently, the energy supply sector for industrial, transportation, and residential applications is dominated by fossil-fuel-based power systems around the globe. However, the two major concerns regarding these power systems are the depletion of limited fossil fuel resources and the emission of greenhouse gases, specifically CO_2 [1–3]. The development of energy-saving systems, investments in new technologies for harnessing renewable energy sources, and legal commitments to the environmental protection plans like net-zero emission pledges are some examples of the main strategies taken by local governments to address the current climate crisis issues. A clean energy system should generally utilize sustainable resources to supply reliable power at a low-levelized cost and high efficiency [4]. Clean energy systems such as fuel cells [5], batteries [6], solar cells [7], wind power [8], geothermal systems [9], biogas [10,11], thermoelectric materials [12], hydrogen energy [13], etc. can offer environmental, economic, and social advantages over the fossil fuels [14,15]. As the lightest and most efficient fuel with the highest energy density, hydrogen can serve the clean energy systems through multiple roles, either as a standalone fuel, chemical energy carrier, or grid-balancing energy storage medium. The thermochemical water-splitting techniques have a significant potential to efficiently convert renewable energy resources

(such as solar energy) into green hydrogen and other valuable chemical energy carriers. The interest in developing these cycles began in the late 1970s, shortly after proposing several types of metal/metal oxide redox loops operating based on high-temperature solar systems and nuclear power sources to produce carbon-free hydrogen fuel.

Hydrogen is considered an energy carrier that can store or deliver a significant amount of energy. The energy density of the hydrogen is nearly three times higher than that of gasoline or diesel with higher HHV (~141.9 kJ/g) and LHV (~119.9 kJ/g). The environmental impact of hydrogen compared to the other fuels can be quantified by the following equations [16,17]:

$$EIF = \frac{kg\ CO_2\ product\ of\ combustion\ reaction}{kg\ fuel} \quad (1)$$

$$GF = \frac{EIF_{max} - EIF}{EIF_{max}} \quad (2)$$

$$HCF = \frac{kg\ H_2\ in\ the\ fuel}{kg\ fuel} \quad (3)$$

where EIF, GF, HCF, and EIF_{max} are the environmental impact factors, greenisation factors, hydrogen content factors, and maximum value of EIF, respectively. As shown in Figure 1, greener energy sources (high GF) have high hydrogen content (high HCF) and more negligible environmental effect (low EIF) [16,17].

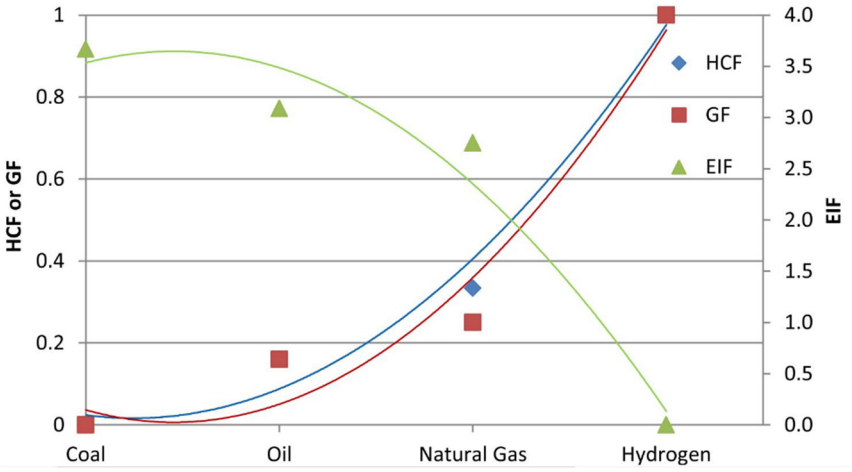

Figure 1. HCF, GF, and EIF of coal, oil, natural gas, and hydrogen (Reproduced with permission from [17], Elsevier: 2015).

Hydrogen can replace fossil fuels in feedstock required for oil refining [18,19], steelmaking [20], commercial and residential heating [21], energy storage and stationary/portable applications [22,23], alternative fuels for automotive diesel engines [24], fuel cell-based combined heat and power plants [25], aerospace applications [26], etc. Unlike fossil fuels, hydrogen must be produced before being used as a clean energy source. The current main hydrogen source comes from burning fossil fuels (>95%) which results in CO_2 emission itself [14]. As reported in 2005, fossil fuel reforming, oil reforming, coal gasification, and water electrolysis produce about 50%, 30%, 18%, and 3.9% of the global H_2 demand, respectively [27,28]. Utilizing fossil fuels for hydrogen production has adverse effects on the environment, climate, and human health; thereby, green technologies for hydrogen production have been developed. However, these technologies suffer from lower effectiveness, high expense, and less quick accessibility than non-green technologies. For instance, hydrogen production from photovoltaic electrolysis costs more than $5 per kg with energy and exergy efficiency of less than 5% [29]. Thus, significant efforts have been invested in

developing an efficient and low-cost hydrogen production technique. Figure 2 illustrates the most important hydrogen applications.

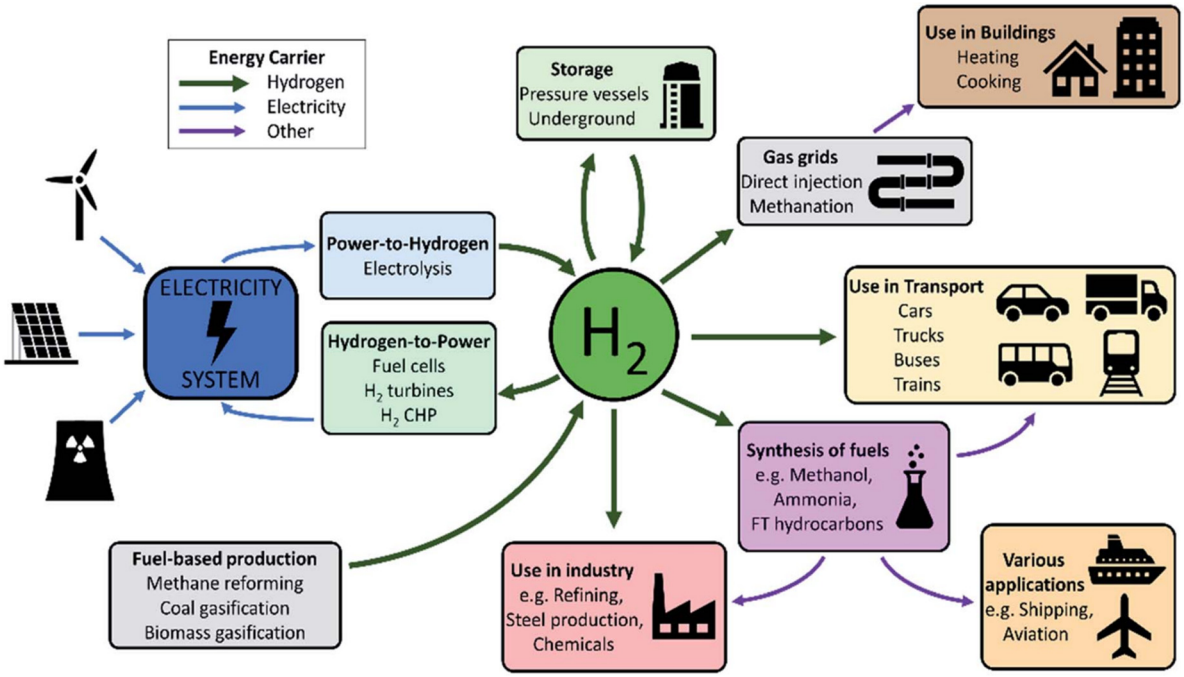

Figure 2. A summary of hydrogen applications [30].

Hydrogen must be separated from its original compound to produce pure hydrogen. Green hydrogen or renewable hydrogen is the term used for the hydrogen that comes from the technologies utilizing renewable energy or biogas for hydrogen production [31]. There are other types of hydrogen indexed by colours, such as blue hydrogen, grey hydrogen, brown hydrogen, black hydrogen, turquoise, etc. Hydrogen is produced using natural gas steam forming, brown or black coal, methane, and so forth [32,33]. There have been significant advances in hydrogen production via various routes such as steam methane reforming (SMR) [30], chemical looping [34], methane thermal cracking coupled with chemical looping combustion [35], water splitting technologies [36], integrated gasification combined cycle (IGCC) [37], hydrogen bioenergy with carbon capture and storage (HyBECCS) [38], etc. The following sections will discuss some hydrogen production methods, emphasizing green technologies.

2. Fossil Fuel-Based Technologies

As mentioned earlier, fossil fuels are the dominant source of producing the required hydrogen for the industry. Due to the high hydrogen content of hydrocarbons, they show great potential for hydrogen production. Hydrocarbon decomposition and pyrolysis have been extensively studied as efficient hydrogen production methods during the past decades. These processes can be promoted using an appropriate catalyst [39]. In what follows, the most critical fossil fuel-based technologies for hydrogen production are briefly discussed.

2.1. Steam Methane Reforming (SMR)

Steam methane reforming or natural gas reforming is the most industrial technology for hydrogen production in which natural gas or other low-boiling hydrocarbon derivatives is the primary feedstock. In the SMR process, natural gas is first de-sulfurized by passing through active carbon and reforming at 700–825 °C in a continuous catalytic process and reacting with steam, finally producing syngas (a mixture of hydrogen and carbon monoxide). Equation (4) shows the strong endothermic reaction of methane and steam [34,40]:

$$CH_4 + H_2O \rightleftarrows CO + 3H_2 \Delta H_{298K} = +206.3 \text{ kJ/mol} \quad (4)$$

The general equation of the reaction between hydrocarbons and steam is as follows:

$$C_nH_m + nH_2O \rightleftarrows nCO + (0.5m + 2)H_2 \quad (5)$$

Syngas is cooled and passed through water-gas shift reactors to increase hydrogen yield and decrease carbon monoxide. As a result, the reaction between CO and steam is slightly exothermic [40,41]:

$$CO + H_2O \rightleftarrows CO_2 + H_2 \Delta H_{298K} = -41.16 \text{ kJ/mol} \quad (6)$$

Finally, gas impurities such as carbon dioxide, water, methane, and carbon monoxide are removed from the flue gas, and the overall chemical process can be given by [40,41]:

$$CH_4 + 2H_2O \rightleftarrows CO_2 + 4H_2 \Delta H_{298K} = +165.2 \text{ kJ/mol} \quad (7)$$

According to thermodynamics, removing carbon dioxide or hydrogen may shift the equilibrium toward the product. Calcia (CaO) can remove carbon dioxide by reacting with it and producing $CaCO_3$, thus, reducing the costs of reactor wall materials and catalyst sintering and coking. This exothermic reaction can also generate the heat needed for the endothermic reaction of the SMR process [40]. The heat required by the endothermic reactions can also be generated by the autothermal (or secondary) reformers (ATR), in which methane oxidation partially supplies the heat in a single chamber [41]. Nickel-based catalysts are the most common materials for reforming the feedstock due to their high performance and cost-efficiency. Other candidates including noble metals (such as Rh, Ru, Pt, Pd, Ir, etc.), transition metals (such as Ni, Co, Cu, Fe, etc.), and oxide supports (such as Ni/MgO, Ru/Mg(Al)O, Ni.Al_2O_3, etc.) have also been investigated for potential application as catalyst [42]. The highest conversion efficiency of the SMR process is about 75–85% [41]. A schematic of the SMR process is shown in Figure 3.

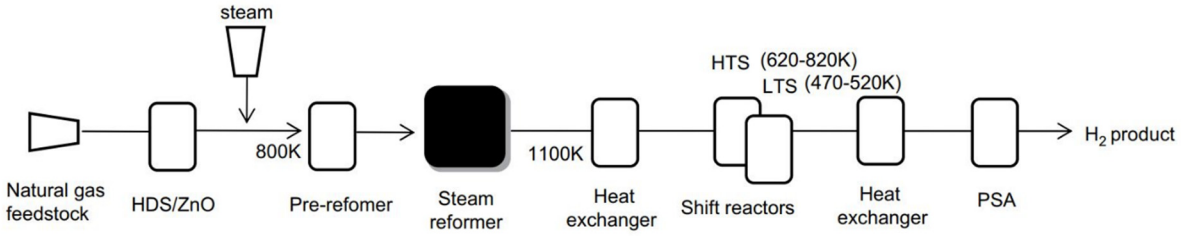

Figure 3. Schematic diagram of the conventional SMR process (Reproduced with permission from [43], Elsevier; 2009).

2.2. Chemical Looping

Chemical looping is an environmentally friendly hydrogen production technology with high energy efficiency and inherent carbon dioxide capture. Oxygen carriers (OCs) constantly circulate between the fuel and air in this process. As a result, the oxidation reaction (Reaction (8)) in the air reactor is exothermic, and the generated heat supplies the energy needed for converting fuel into CO_2 and H_2O (Reaction (9)) in the second chamber, thereby reducing the energy consumption (Figure 4) [34,44].

$$M_xO_{y-1} + \frac{1}{2}O_2 \rightleftarrows M_xO_y \quad (8)$$

$$(2n + m)M_xO_y + C_nM_{2m} \rightleftarrows (2n + m)M_xO_{y-1} + mH_2O + nCO_2 \quad (9)$$

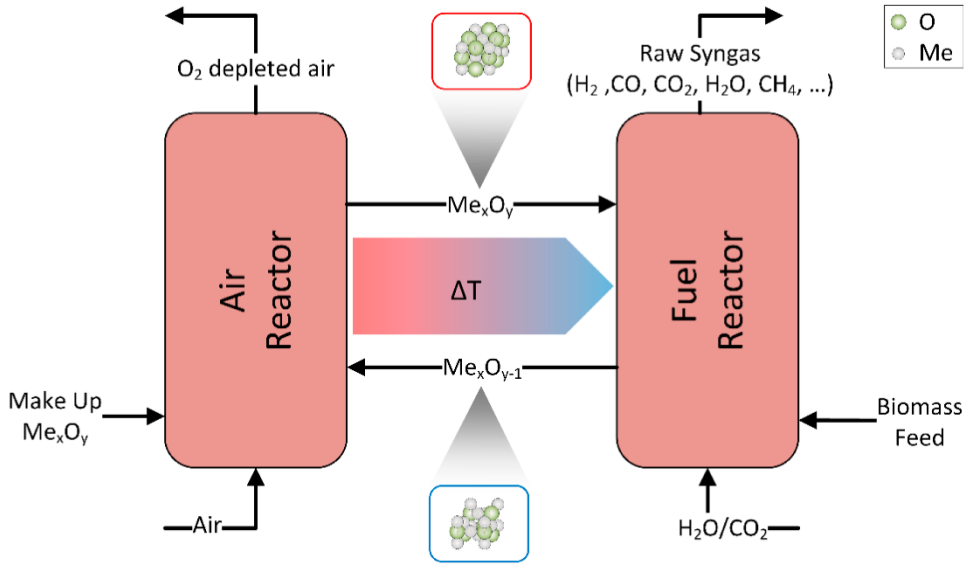

Figure 4. Schematic description of chemical looping process [45].

Generally, the following reaction may happen in air and fuel reactors [44,46]:

$$in\ air\ reactor \begin{cases} C + O_2 \rightleftarrows CO_2 \\ 2C + O_2 \rightleftarrows 2CO \\ 2Ni + O_2 \rightarrow 2NiO \end{cases} \quad (10)$$

$$in\ fuel\ reactor \begin{cases} C_2H_5OH + H_2O(\overset{Ni}{\rightleftarrows})2CO + 4H_2 \\ C_2H_5OH + 6NiO \rightarrow 6Ni + 2CO_2 + 3H_2O \\ CO + H_2O \rightleftarrows CO_2 + H_2 \end{cases} \quad (11)$$

To produce hydrogen from chemical looping, chemical looping reforming (CLR) and chemical looping hydrogen (CLH) have been proposed [34]. CLR is a relatively new method to convert liquid, solid, or gaseous fuel into hydrogen, and according to the characteristics and principles, CLR can be classified into three types; namely, steam reforming integrated with chemical looping combustion (SR-CLC) or CLR(s), auto thermal chemical looping reforming or CLR(a), and chemical looping steam methane reforming (CL-SMR or CLRM) or two-step steam methane reforming. In CLR(s), the steam reforming tubes are [34,47] metal-based materials such as Ni-, Fe-, Cu-, Ce-, Co-, and Mn-based materials have been known to be suitable oxygen carriers [48]. The most extensively studied oxygen carriers used in this process are nickel-based materials with superior redox properties and low cost. However, they suffer from metal sintering and coke deposition [48,49]. To overcome these drawbacks, bimetallic oxygen carriers such as Ni-Fe, Fe-Co, Cu-Ni, Fe-Ca, Fe-Cu, Co-Ni, etc. [34,50–53] as well as oxide perovskite materials with a general formula of ABO_3 (such as $LaNiO_3$, $CaMn_{0.375}Ti_{0.5}Fe_{0.125}O_{3-\delta}$, etc.) [54,55].

2.3. Integrated Gasification Combined Cycles (IGCC)

Integrated gasification combined cycle (IGCC), one of the most developed carbon capture technologies with high energy efficiency and relatively low costs, combines a coal gasification unit with a gas turbine-steam power plant to achieve higher efficiency and performance [56–58]. In IGCC, the solid or liquid feedstock is partially oxidized. It produces syngas followed by purifying it from dust and hydrogen sulphide which is then sent to the combined cycle gas turbine (SCGT) to generate power. Producing one MWh of electricity using natural gas and coal resulted in high carbon dioxide emissions of about 350–400 and 800–900 kg, respectively [59,60]. The mitigation costs of carbon dioxide in 2030 are predicated to be about 11, 26, and 19 €/t for IGCC, natural gas combined cycle (NGCC), and pulverized coal (PC) power plants [61]. IGCC can generate 400 MW electricity with

90% rate of carbon capture [59,62]. It has been reported that using the off-gases from the gas turbine as an energy source can enhance the power generation capacity [63]. In this context, Gholamian et al. [64] studied an improved IGCC system comprised of biomass gasification, a supercritical carbon dioxide cycle, a gas turbine cycle, and a water heater. They showed that the exergy efficiency reached a high value of about 40.10%. Soltani et al. [64] carried out the energy and exergy analyses of the integrated biomass gasification and gas turbine combined cycle and reported that adjusting the pressure ratio can maximize the thermal efficiency. A comprehensive study on the state-of-the-art IGCC technologies as well as the uncertainty, dynamics, controllability, etc. can be found elsewhere [63]. Overall, despite all of the advances in optimizing the IGCC process, design complexity and higher costs of IGCC plants in comparison with a conventional plant limit their application [61].

2.4. Biomass Gasification

Biomass gasification is another mature technology for hydrogen generation by converting biomass or fossil-based carbonaceous materials to syngas without combustion and under a controlled process. Compared with fossil fuels, biomass is less expensive and more widely available, reducing greenhouse gas emissions and high energy efficiency [65,66]. Biomass gasification involves a thermochemical process at high temperatures (~900 °C) and low pressure. The main steps include drying the feedstock, pyrolysis of the feedstock, and a reaction part including oxidation, reduction, and cracking [67–69]. The products are carbon monoxide, carbon dioxide, methane, and hydrogen. To maximize the hydrogen content, purification with water-gas shift (WGS) reaction, carbon capture technologies, separation stages for syngas purification, etc. [69–71]. The main drawback of this method is releasing tar that should be removed from the syngas, which is expensive and reduces the overall efficiency [67]. Over the past years, many studies have been carried out to optimize the operating conditions. A novel steam/air biomass gasification combined cooling, heating, and power generation system with solar energy has been proposed by Wu et al. [72]. They reported that using solar-driven biomass gasification, the primary energy efficiency and the increment rate of electric power improved about 5.98% and 5.91%, respectively. However, the new design did not increase the overall annual electricity, cooling, and heating profits. Zhang et al. [73] improved hydrogen yield, energy consumption saving, and overall efficiency of a biomass gasification system by incorporating an autothermal calcia looping. A novel approach including a biomass gasification system integrated with thermoelectric generators with high energy and exergy efficiencies has been proposed by Ishaq et al. [74]. Energy and exergy analysis of biomass gasification were studied by Ebrahimi and Ziabasharhag [75] who proposed a new configuration including of a tri-generation of liquid natural gas, power, and heat. Overall, despite all of the recent progress in developing new technologies with higher efficiency, it is still economically unfavourable compared to methane/natural gas steam reforming.

2.5. Other Fossil Fuel-Based Technologies

The energy density of Bio-oil, which is a mixture of organics such as aldehydes, carboxylic acids, furans, alcohols, phenolics, ketones, etc., is larger than biomass [76]. The tendency for coking and reform is affected by the molecular structure. Due to the lack of aliphatic carbon chains, which should be cracked during the process, formic acid and methanol can be reformed at low temperatures. However, acetic acid, acetone, ethanol, or acetaldehyde need much higher temperatures and may produce a significant amount of coke deposits [77]. The most prevalent catalysts used in this process are Cu/Al_2O_3, Ni/Al_2O_3, and Co [78]. Methanol steam reforming is a method that can produce hydrogen from biomass and carbon dioxide. Due to the high H:C ratio and the absence of C-C bonds, methanol shows a lower tendency to coke formation and by-products compared to ethanol [79]. The most common catalysts for methanol steam reforming are Cu-based compounds such as Mg-doped Cu-Al spinels [80], $CuPd/TiO_2$ [81], $CuFeO_2$-CeO_2 [82], Cu/ZrAl-based [83], etc. Due to the great potential of alkanes in large-scale chemical indus-

tries, one of the relatively new technologies for hydrogen production is alkanes (such as ethane, propane, etc.) dehydrogenation in a catalytic membrane reactor in which hydrogen can be produced in the reaction zone and separated from the alkene-containing flow via a membrane [84,85]. Dehydrogenation of propylene has also been investigated during the past decade [86]. However, several aspects of this process need to be further studied to assess its hydrogen yield and cost-effectiveness. Ethanol steam reforming can also be used for hydrogen production and a Ni-based catalyst. However, the most challenging issue with ethanol steam reforming is carbon formation. Carbon formation in this process can be prevented by controlling the particle size of the metal [78]. Due to the suppression of methanation reaction, the promoted catalysts show higher hydrogen production efficiency than the unpromoted ones. These promoters include Na, Mg, La, Zr, Ce, K, Zn, etc., which can be used on Co/Al_2O_3, Co/CeO_2, Ni/CeO_2, $Pt/m\text{-}ZrO_2$, etc. [87–89].

3. Green Hydrogen Technologies

One of the carbon-free technologies for hydrogen production is water splitting. It has been extensively investigated as a promising and effective approach for hydrogen production, thus mitigating the energy crisis and reducing environmental pollution. However, the decomposition of water into hydrogen and oxygen requires very high temperatures of about 2500 °C. Thus, the need for technologies that can operate at lower temperatures is of great importance to reduce the costs [90]. Several promising routes have been proposed for hydrogen production through green technologies such as biological processes (such as CO gas-fermentation, dark fermentation, etc.), electrical (such as alkaline electrolysis cell, anion exchange membrane electrolysis cell, proton exchange membrane electrolysis cell, solid oxide electrolysis cell, etc.), photonic (bio-photolysis, photofermentation, etc.), thermochemical, etc. [78]. Thermochemical cycles such as sulfur-iodine [91], hybrid sulfur [92], sulfur ammonia [93], copper-chlorine [94], etc. have many advantages over methods such as recovering and recycling all the chemicals except water into the cycle, moderate operating temperatures, relatively low power input requirement, heat and water are the only inputs, [95,96]. Water splitting methods based on solar energy can be divided into three main categories:

- Thermochemical routes such as single- and multi-step water splitting cycles;
- Photochemical routes such as photoelectrochemical, photocatalytic, photobiological, etc.;
- Electrochemical routes such as PV-electrolysis [93,97].

Each of the cycles, as mentioned above, has its merits and demerits. For example, PV-electrolysis is one of the most developed methods with a maximum solar-to-electric energy conversion efficiency of about 32% for single-crystalline Si, $CuIn_{1-x}Ga_xSe_2$, CdTe, GaAs [93]. On the other hand, water electrolysis is a matured technology with an electric-to-hydrogen energy conversion efficiency of about 70–80%. It has been reported that the highest solar-to-hydrogen energy conversion efficiency of PV-electrolysis is in the range of 15–20% [93]. Direct conversion of solar energy into hydrogen using the photoelectrochemical route is a single-step method with relatively low solar-to-hydrogen energy conversion efficiency (<10%). Photobiological and photocatalytic cycles have also been under development [93]. Generally, thermochemical water splitting cycles are divided into two classes according to the operating temperature:

- Low-temperature cycles with an operating temperature below 1100 °C, such as sulfur-iodine, hybrid sulfur, hybrid copper chloride, etc.
- High-temperature cycles with an operating temperature above 1100 °C, such as Zn/ZnO, FeO/Fe_3O_4, manganese oxide-based, ferrite cycles, etc. [98]

3.1. Low-Temperature Cycle

3.1.1. Sulfur-Iodine Cycle

The sulfur-iodine cycle (S-I cycle) is a thermochemical water-splitting process that the General Atomics Corporation first developed in the mid-1970s [99]. It has been extensively studied and developed in the past decade, especially by the French Commissariat à

L'Énergie Atomique in France, the Institute of Nuclear Energy Technology in China, the Korean Institute of Energy Research in Korea, the Japan Atomic Energy Agency in Japan, etc. [100]. Generally, the S-I cycle is composed of three steps as given below [101,102]:

$$2H_2O(l) + SO_2(g) + I_2(s) \rightarrow H_2SO_4(aq) + 2HI(aq). \ \mathrm{T} = 20\text{–}120\ ^\circ\mathrm{C}. \quad \Delta\mathrm{H} = -75 \pm 15\ \mathrm{kJ/mol} \tag{12}$$

$$H_2SO_4(g) \rightarrow \frac{1}{2}O_2(g) + SO_2(g) + H_2O(g). \quad \mathrm{T} = 850\ ^\circ\mathrm{C}. \Delta\mathrm{H} = 186 \pm 3\ \mathrm{kJ/mol} \tag{13}$$

$$2HI(g) \rightarrow H_2(g) + I_2(g). \quad \mathrm{T} = 450\ ^\circ\mathrm{C}. \quad \Delta\mathrm{H} \sim -12\ \mathrm{kJ/mol} \tag{14}$$

The first reaction occurs at about 100 °C and is an exothermic reaction between solid iodine and sulfur dioxide in an aqueous media, producing hydriodic and sulfuric acid (Bunsen reaction) [103]. The product is an immiscible aqueous phase called the HI_x phase (composed of HI, H_2O, and I_2) and sulfuric acid (SA) phase (composed of H_2SO_4 and H_2O). The efficient separation of these phases has been reported that the efficient separation can achieve the highest efficiency. SA impurities (such as HI) and HI_x impurities (such as H_2SO_4) may have side reactions, and removal of these impurities can further improve the overall efficiency [100]. To prevent cross-contamination in each phase, excessive iodine can be introduced into the liquid–liquid separator [104]. Reaction (13) is a high-temperature endothermic reaction of sulfuric acid decomposition and usually takes place in bayonet-type HEX/reactors at about 850–900 °C [101]. In this step, the SA concentration reached about 90 wt.% by distillation followed by decomposition of sulfuric acid in two steps; (a) decomposition of sulfuric acid to H_2O and SO_3; and (2) decomposition of SO_3 to O_2 and SO_2. Then, H_2O and SO_2 are cooled down to about 120 °C and recycled into Reaction (12), and O_2 is stored in the tanks [100]. Reaction (14) involves the endothermic decomposition of hydriodic acid to gaseous iodine and hydrogen at about 400–500 °C [101,105,106]. Reaction (14) can be divided into two steps: (1) HI_x is separated to HI_x solution of azeotrope HI (~15.7 mol.%) and HI gas; and (2) decomposition of HI to H_2 and I_2 in a decomposition reactor [107]. Therefore, the net reaction can be written as follows:

$$2H_2O(l) \rightarrow 2H_2(g) + O_2(g) \tag{15}$$

A schematic process diagram of the S-I cycle for hydrogen production is represented in Figure 5.

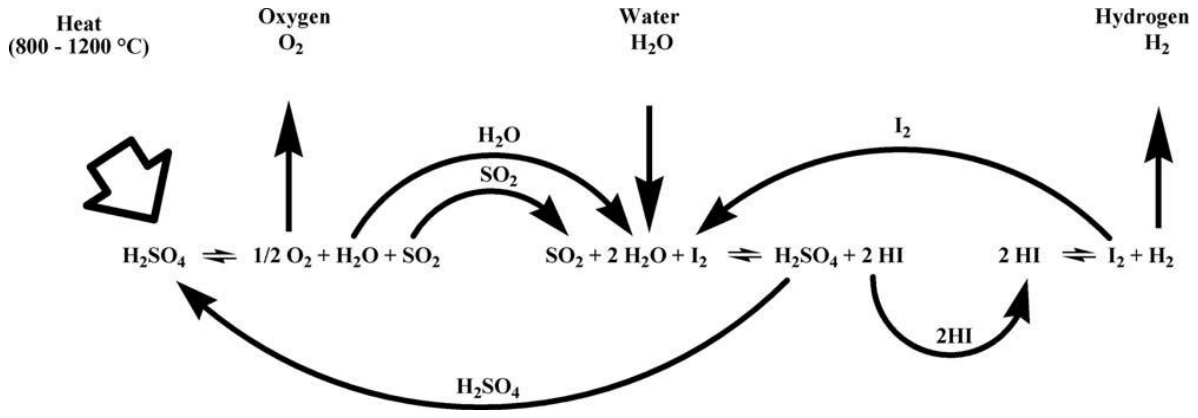

Figure 5. A sample process flow diagram of the S-I cycle [108].

The efficiency of the S-I cycle increased with increasing temperature and reached about 52 and 60% at 900 and 1000 °C, respectively [100,101]. It has been reported that the efficiency of the S-I cycle is amongst the highly efficient hydrogen production cycles [103]. However, S-I cycle technology suffers from some drawbacks. In the phase equilibrium between H_2O and HI, the HI-H_2O azeotropic solution is deficient (about 15.7 mol.%) [107]. Therefore, the efficiency of the Bunsen reaction may be reduced by the incoming oxygen [109]. Another

disadvantage of the S-I cycle is phase separation in traditional Bunsen reactions, reducing the overall efficiency [110]. Introducing excessive iodine for improving the separation efficiency of HI from sulfuric acid may cause problems such as clogging the pipes [100]. In addition, the decompositions of hydriodic and sulfuric acid create a corrosive environment. The aggressive chemical environment is one of the most significant drawbacks of the S-I cycle because it can have a significant adverse effect on the reactors [101,103]. Reactor materials and other materials used in the cycle may corrode because H_2SO_4 and HI are corrosive compounds. Thus, these corrosive materials should be handled carefully [111]. The most important properties of catalysts are high catalytic activity, high catalyst stability, cost-effectiveness, etc. [111].

Numerous researchers have focused their studies on overcoming the issues mentioned above. Optimizing the feed to liquid-liquid separator conditions and minimizing the impurities can lead to a solution in the range of iodine solubility and above the azeotropic condition [109]. Zhu et al. [107] optimized the solution composition and the operating temperature of the S-I thermochemical cycle to efficiently separate the liquid-liquid phase in the Bunsen section of a quaternary solution composed of H_2SO_4 HI, I_2, and H_2O (the secondary reactions were neglected in the experiments). According to their results, excessive iodine was more vital than increasing the operating temperature. The iodine content and temperature improved the separation characteristics and decreased the impurities. The optimum operating temperature and the I_2/H_2SO_4 molar ratio were found to be in the range of 70–85 °C and 2.45–3.99, respectively, resulting in obtaining a hyper-azeotropic HI concentration. To prevent phase separation in the Bunsen reaction section, electrochemical cell, chemical precipitation, nonaqueous solvents, and electrolysis of $HI/H_2SO_4/H_2O$/toluene mixture has been proposed [112–114]. Optimization of the Bunsen reaction in the S-I cycle has been profoundly investigated by Zhang et al. [114] and can be used as a guideline for the Bunsen step of the process.

Yu et al. [115] developed a microporous membrane resistant to SO_3, which consisted of α-alumina as the membrane support, zirconia-silica as the intermediate layer, and bis(triethoxysilyl)ethane-derived organosilicons sol as the top layer to be used in SO_3/O_2 separation. The membranes with a large pore of zirconia-silica and high Si:Zr ratio showed high chemical stability against SO_3 and high O_2/SO_3 selectivity of 10. Park et al. [116] proposed a modified S-I cycle and conducted the economic evaluation, socio-economic analysis, thermodynamic feasibility analysis, and risk assessment. The modified S-I cycle was composed of fewer reactions than a typical S-I cycle and employed a steam boiler instead of a nuclear heat source. The modified S-I cycle's verification and thermodynamic feasibility were carried out according to the second law of thermodynamics. The HI decomposition and the Bunsen reactions were feasible at temperatures higher and lower than 225 °C, respectively.

In comparison with the S-I cycle with a nuclear heat source, the results of the techno-economic analysis of the modified cycle showed that the capital and operating costs were reduced by 40% and 29%, respectively. Furthermore, the modified S-I cycle's failure rate and social health cost were about 64% and 41% less than the S-I cycle, respectively. Overall, the results revealed that the modified cycle is a suitable alternative process to the S-I cycle with improved cost efficiency and safety.

Due to the HI decomposition rate's low equilibrium conversion rate on the S-I cycle's overall efficiency, some catalysts have been used to reduce the activation energy and improve the decomposition rate of this process [117]. Several metallic and non-metallic candidates have been proposed to be used as a catalyst. In the case of metallic catalysts, Kim et al. [118] studied the effect of decomposition temperature, Pt content, and the amount of absorbed iodine in Pt/C-based catalysts on the decomposition rate of HI. They reported that 5 wt.% Pt loading resulted in the highest decomposition rate of about 22.5% HI at 550 °C and remained constant at higher Pt contents. HI decomposition rate increased with increasing decomposition temperature from 6% at 450 °C to 16% at 550 °C. The results showed that the adsorbed iodine decreased with increasing Pt content and decomposition

temperature. Thus, removing adsorbed iodine is critical at lower temperatures to retain a suitable catalytic activity. The same results have been reported for Pt content in Pt/Al_2O_3 catalyst [119]. Other types of metallic catalysts such as Pt/CeO_2 [120], Ni/CeO_2 [121], carbon nanotubes supported palladium catalyst (with equilibrium conversion of about 23.7% at 550 °C for Pd(3%)CNT sample) [122], etc. have also been investigated for their potential application as HI decomposition catalyst. Tyagi et al. [90] prepared carbon from rice and used it to support Pt catalyst to promote HI decomposition reaction. The carbon-supported catalysts enhanced the liquid phase HI decomposition and were chemically, structurally, and catalytically stable under the operating conditions. Different types of supports have been proposed, such as zirconia [123], ceria [120], graphite [124], alumina [119], etc. However, despite all advances in metallic catalysts, their high costs (Pt-based), low catalytic efficiency (Ni-based), etc., hinder their large-scale applications.

Due to the challenges mentioned above, non-metal catalysts have been developed during the past decades. Amongst the non-metallic catalysts, activated carbon (AC) has attracted great interest. It has been reported that high specific surface area and carbon content improve the catalytic performance of AC catalysts [125]. Wang et al. [126] concluded that the main active constituents are the unsaturated carbon atoms. Due to the high tendency of unsaturated oxygen atoms to integrate oxygen, lower oxygen contents result in higher unsaturated carbons. Consequently, the low area density of oxygen promotes HI conversion. Rong et al. [117] investigate the effect of specific surface area and pore structure of coconut shell-activated carbon catalysts. The highest catalytic activity was achieved for the sample with hierarchical pore structure (with macro- and micro-pores), while too low or too high micropores reduced the catalytic efficiency. The results implied that the catalyst with micropore proportion close to 50% and high specific surface area exhibits the highest HI decomposition efficiency and hydrogen yield. Lin et al. [127] also reported that a higher surface area and pore diameter could improve the catalytic activity, while the ash content is detrimental to improving the HI conversion efficiency. Finally, Li et al. [102] studied the effect of N-doping on the decomposition efficiency of activated carbon catalysts. They reported that increasing N content facilitates HI decomposition by enhancing the HI molecules' chemisorption on carbon, and the sample containing 6.006% N showed the highest HI conversion of about 22.84%. N-6 structure exhibited the higher HI chemisorption than N-5 and N-Q structure. However, the highest HI chemisorption was achieved when all N-containing functional groups were present in the sample simultaneously.

Some catalysts have been proposed to increase the rate of SO_3 to SO_2 decomposition reaction. The most active catalysts for this process are the Pt-based catalysts such as $Pt\text{-}Al_2O_3$, mainly due to their low activation energy (~70.7–73.1 $kJ{\cdot}mol^{-1}$) and high sulfur trioxide decomposition rates (>80%) [128,129]. Highly active and stable Pt-loaded anatase catalysts are a new type of catalyst with high catalytic activity without anatase to rutile transformation, decreasing the catalytic activity. The increased activity of Pt on anatase is related to the abundance of metallic platinum, which facilitates the dissociative adsorption of sulfur trioxide as well as SO_2 and O_2 removal from the surface. A slight activity loss has been observed in these catalysts attributed to the slow sintering and loss of platinum [130]. The catalytic activity of non-platinum-based catalysts has also been studied. Kawada et al. [131] fabricated Ce-V oxide catalysts supported on mesoporous silica through the wet impregnation method and studied their catalytic activity. The $Ce\text{-}V/SiO_2$ catalysts with Ce:V ratio of 0.9 showed the highest catalytic activity. The catalytic performance of the Ce-V oxide catalysts with $CeVO_4$ nanoparticles (~13 nm) dispersed in the bimodal mesoporous silica support showed significantly higher turnover frequency than the unsupported catalysts with an average particle size of 600 nm, mainly due to the higher specific surface area of the supported catalysts. $CuO\text{-}CeO_2$ based catalysts supported on $SiC\text{-}Al_2O_3$ showed high activity and stability and decreased the decomposition temperature to about 625 °C. The high catalytic activity of the catalyst was attributed to a large number of defective sites and higher sulfur trioxide adsorption [132].

3.1.2. Hybrid Sulfur Cycle

As shown in Figure 6, the Westinghouse cycle or Hybrid Sulfur (HyS) cycle is a two-step process for hydrogen generation using thermochemical and electrochemical technologies widely investigated for large-scale hydrogen production. The thermochemical and electrochemical steps occur at temperatures higher than 800 °C and 80–120 °C, respectively [133].

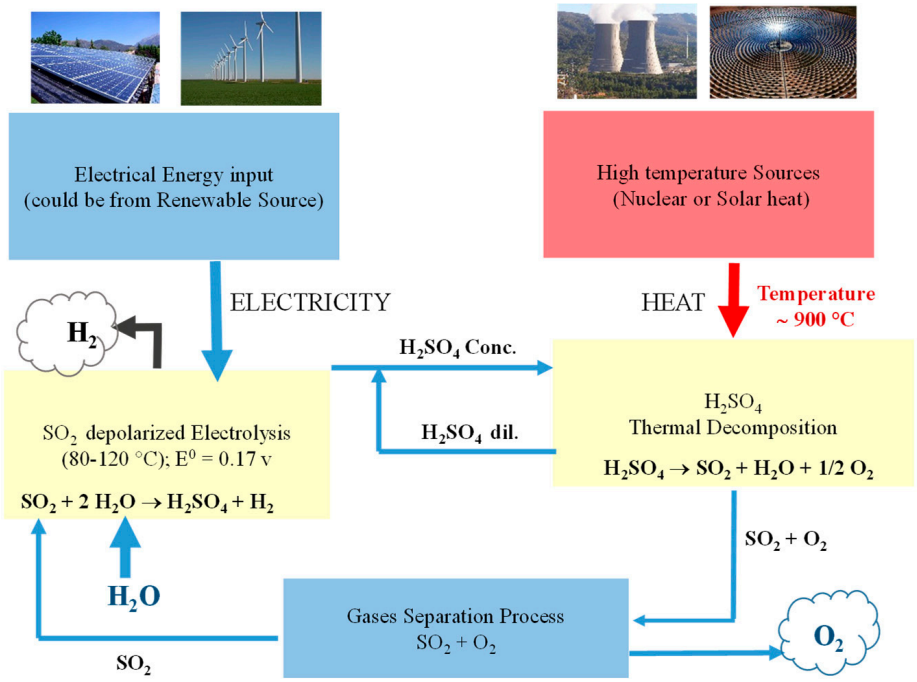

Figure 6. Hybrid Sulfur cycle [108].

The following reaction can be written for this cycle [133,134]:

$$H_2SO_4(aq) \rightarrow H_2O(g) + \frac{1}{2}O_2(g) + SO_2(g) \text{ (Thermochemical step)} \quad (16)$$

$$SO_2(aq) + 2H_2O(l) \rightarrow H_2(g) + H_2SO_4(aq) \text{ (Electrochemical step)} \quad (17)$$

Reaction (16) is an endothermic reaction in which the produced oxygen is extracted from the process, while the SO_2 produced in this step is circulated within the process to drive the second step. On the other hand, reaction (17) is an exothermic reaction, and the final products of the electrochemical oxidation of sulfur dioxide are sulfuric acid and hydrogen. At the end of this process, hydrogen is separated, purified, and extracted from the process, while sulfuric acid is re-circulated within the process [133,135]. This cycle consists of three significant steps: (1) vaporization and decomposition of H_2SO_4, (2) separation of SO_2/O_2, and (3) SO_2 anode-depolarized electrolysis. The decomposition of sulfuric acid can be divided into four processes given below [92,134]:

(a) The concentration of sulfuric acid by evaporating off the water;
(b) Evaporating of concentrated and still liquid H_2SO_4;
(c) Dissociation of gaseous acid into water vapour and SO_3 at T = 350–400 °C;
(d) Decomposition of SO_3 to SO_2 at T = 700–1000 °C.

SO_2/O_2 separation happens at low temperatures (−45 °C) and high pressure (20 bar), where sulfur dioxide is liquid and can be separated from the oxygen gas. The amount of sulfur dioxide sent to the electrolyzer is essential in increasing hydrogen production. Thus, this step should be optimized, i.e., by producing a maximum amount of liquid sulfur dioxide and oxygen gas [92].

The specific section of the HyS cycle is the electrochemical step in which sulfur dioxide oxidizes and produces sulfuric acid and hydrogen ions (H^+) at the anode side. Water and sulfur dioxide are used to depolarize the anode, which the electrolyzer usually works in the temperature range of 25–140 °C. The following reactions take place in this step [92,134,135]:

$$H_2SO_4(g) \rightarrow H_2O(g) + SO_3(g) \text{ T} = 350\text{–}400\ ^\circ\text{C};\ \Delta H^\circ = +98\ \text{kJ}\cdot\text{mol}^{-1} \quad (18)$$

$$SO_3(g) \rightarrow \frac{1}{2}O_2(g) + SO_2(g) \text{ T} = 700\text{–}1000\ ^\circ\text{C};\ \Delta H^\circ = +99\ \text{kJ}\cdot\text{mol}^{-1} \quad (19)$$

The configuration of the electrochemical component is either a vapour-fed or a liquid-fed electrolyzer. In the liquid-fed design, first developed at the Savannah River National Laboratory, liquid sulfur dioxide and water mixture were oxidized at the anode side, forming sulfuric acid, hydrogen protons, and electrons. Then, the protons migrate to the cathode side by passing through the membrane and producing H_2 by recombining with external electrons [136,137]. Sulfur dioxide crossover through the membrane is one of the most critical issues associated with liquid-fed design. To overcome this problem, proton exchange membranes (PEMs), such as sulfonated polybenzimidazole (s-PBI) with cell potential of about 0.6–0.7 V at a current density of 500 $\text{mA}\cdot\text{cm}^{-2}$, have shown great potential to prevent sulfur dioxide crossover and accumulation [138,139]. The vapour-fed design has been developed by a collaboration between the University of South Carolina and Savannah River National Laboratory [135]. In this configuration, dry vapour, sulfur dioxide, and water are fed to the anode and cathode sides, respectively. Due to the pressure gradient and water activity difference, water diffuses through the membrane to the anode side and is then re-transported to the cathode side due to electro-osmotic drag [135]. The standard cell potential for the electrochemical step is about −0.158 V at room temperature, which is about 13% of the water electrolysis potential (~−1.229 V) [137,140].

The first step occurs spontaneously, but the reaction rate of SO_3 reduction to SO_2 is low and requires some catalysts such as Pt, Fe_2O_3, Cr_2O_3, NiO, etc. [141]. An issue associated with this step is the kinetic overpotential of sulfur dioxide oxidation reaction, which has been addressed by using Pt as the baseline catalytic formulation [142] or Au nanoparticle catalysts with higher current density and stability than the Pt ones [140]. Kim et al. [143] prepared Fe/Al and Fe/Ti binary metal oxide catalysts via the co-precipitation method and reported that increasing Fe content improved the catalytic activity. They claimed that the decomposition of SO_3 on metal oxides occurs in two steps: (1) the formation of metal sulphates and (2) the decomposition of metal sulphates. Corgnale et al. [135] reviewed the sulfuric acid decomposition processes for thermochemical water splitting methods of hydrogen production. They concluded that some metals such as Cr, Ce, U, Mn, and Ni could form stable sulphates at elevated temperatures. Thereby, they are not suitable catalysts for sulfuric acid decomposition. Due to the formation of $Al_2(SiO_4)_3$, alumina can poison Pt-based catalysts. Some catalysts such as vanadium pentoxide and chromia can act as reverse catalysts and coat colder walls. Oxide materials such as Fe_2O_3 and CuO can be used for high-temperature and low-pressure situations. They concluded that the Pt/$BaSO_4$-TiO_2, Pt/TiO_2, Pt/ZrO_2, and Pt/SiO_2 could be considered the most suitable catalysts with the highest catalytic performance. As can be found from these reports, among the numerous candidates which can be used as the catalyst for the decomposition reactions, Pt-based compounds still show the highest catalytic performance.

Pt-based catalysts are among the first catalysts used for the electro-oxidation of SO_2. Pure black platinum possesses a high catalytic activity with about 0.5 $\text{A}\cdot\text{cm}^{-2}$ at 0.7 V [144]. The mechanism of SO_2 oxidation on Pt is an electrotransfer-electrochemical and mass-diffusion controlled process at potentials lower than the potentials needed for the oxidation of platinum (0.42 V). At the same time, the chemical reaction between anodically-formed oxide and sulphite occurs at higher potentials [145]. Despite all the advantages of Pt-based catalysts, the high price of platinum is a great disadvantage of Pt-based catalysts. Thus, the combination of platinum with other metals has also been investigated. Falch et al. [146] synthesized bimetallic Pt_xPd_y thin-film catalysts deposited on a Si wafer and reported that

Pt_3Pd_2 and $PtPd_4$ showed the highest activity. In another attempt, they studied the effect of thermal annealing on the performance of Pt_3Pd_2 thin film [147]. The surface smoothness deteriorated when the annealing temperature surged from 600 °C to 900 °C. It was found that the electrochemically active area decreased with the annealing process. The decrease in the active area for the Pt_3Pd_2 thin film was more than the Pt catalyst, and the difference increased with increasing annealing temperature. Later, they developed a co-sputtered $Pt_xPd_yAl_3$ film and found that adding another metal has a significant effect on improving the electrocatalytic performance. Zhang et al. [148] synthesized demetallized Pt_xNi_y/C catalysts via the organic-sol method and compared the properties of these catalysts with Pt/C catalysts. Nickel doping increased the electron vacancies and compressed platinum lattice, improving the catalytic activity and catalyst stability. The current density of Pt_1Ni_3/C was 80% higher than that of Pt/C catalyst after 4 h of electrolysis. Xue et al. [149] investigated the electrocatalytic activity of Pt-based bi-metallic compounds including Pt-Pd/C, Pt-Rh/C, Pt-Ru/C, Pt-Ir/C, and Pt-Cr/C catalysts and reported that the 60 wt.% Pt-Cr/C with Pt:Cr ratio of 1:2 showed the highest electrocatalytic activity for SO_2-depolarized electrolysis.

Further chromium content decreased the electrolysis performance. Xu et al. [150] improved the SO_2 electro-oxidation using a $Pt/CeO_2/C$ composite catalyst. Ceria addition increased the catalyst's active area from 429.10 $cm^2 \cdot mg^{-1}$ Pt for Pt/C to about 810.60 $cm^2 \cdot mg^{-1}$ Pt for $Pt/10CeO_2/C$ catalyst, mainly due to the increased oxygen provided by ceria. Gold-based compounds have also been investigated as potential catalysts in the HyS cycle. As gold surface oxide films can dissolve easier in acid solutions, activation of Au-based catalysts is easier than Pt-based ones. However, substrate chemisorption properties strongly affect the rate of SO_2 oxidation and participation of O, OH, or H species. Thereby platinum is more promising than gold due to its higher rate of these processes [144]. Palladium is another noble metal used as a catalyst for SO_2 oxidation that exhibits a better catalytic activity than platinum, mainly due to its higher limiting current density. However, they are less stable compared to Pt-based catalysts [142].

Jayakumar et al. [151] compared Nafion and sulfonated polybenzimidazole (s-PBI) proton exchange membranes in the HyS electrolyzer. While the conductivity of s-PBI did not decrease at low water content and can be used in the temperature range of 100–200 °C, Nafion could not be used at high temperatures, and its conductivity decreased under a highly acidic situation. s-PBI membranes can operate at high acid concentrations, but their kinetics and performance should be further improved [139]. Carbon supports can achieve the highest currents; however, the most promising catalysts to be used in the HyS cycle are Pt-based compounds, but their performance should be at least 0.5 $A \cdot cm^{-2}$ at 0.6 V for full-scale application.

3.1.3. Sulfur Ammonia Cycle

The sulfur ammonia cycle is a four-stage hybrid thermochemical cycle that uses long and short wavelength-solar spectrum to drive thermal processes and hydrogen using photolysis. The main four steps of this cycle are given below [93]:

$$SO_2 + 2NH_3 + H_2O(l) \rightarrow (NH_4)_2SO_3 \text{ chemical absorption} \quad (20)$$

$$(NH_4)_2SO_3 + H_2O \rightarrow (NH_4)_2SO_4 + H_2 \text{ photochemical} \quad (21)$$

$$(NH_4)_2SO_4 + X \rightarrow 2NH_3(g) + XSO_3(s) + H_2O \text{ thermal} \quad (22)$$

$$XSO_3 \rightarrow SO_2 + X + \frac{1}{2}O_2 \text{ thermal} \quad (23)$$

X is a mediator compound involved in oxygen evolution sub-cycles of Reactions (22) and (23). Two types of X have been studied so far:

(a) Alkali metal sulphates such as sodium sulphate, potassium sulphate, caesium sulphates, etc.
(b) Metal oxide such as ZnO, MnO, etc.

The fundamental five steps of the metal sulfate-pyrosulfate sub-cycle are given below (based on S, N, H, K, and O) [135,152,153]:

$$SO_2(g) + 2NH_3(g) + H_2O(l) \rightarrow (NH_4)_2SO_3(aq) \ \mathrm{T} = 25\text{–}50\ ^\circ\mathrm{C} \quad (24)$$

$$(NH_4)_2SO_3(aq) + H_2O(l) \rightarrow (NH_4)_2SO_4(aq) + H_2 \ \mathrm{T} = 80\text{–}150\ ^\circ\mathrm{C} \quad (25)$$

$$(NH_4)_2SO_4(aq) + K_2SO_4(l) \rightarrow 2NH_3(g) + K_2S_2O_7(l) + H_2O(g) \ \mathrm{T} = 400\text{–}450\ ^\circ\mathrm{C} \quad (26)$$

$$K_sS_2O_7(l) \rightarrow SO_3(g) + K_2SO_4(l) \ \mathrm{T} = 790\ ^\circ\mathrm{C} \quad (27)$$

$$SO_3(g) \rightarrow SO_2(g) + \frac{1}{2}O_2(g) \ \mathrm{T} = 850\text{–}1200\ ^\circ\mathrm{C} \quad (28)$$

Reactions (24) to (28) are chemical absorption, electrolytic oxidation, adiabatic mixing, stored thermal and electric heat processes, respectively [152]. The separation of oxygen from sulfur dioxide occurs in Reaction (24), where sulfur dioxide is absorbed in water [152]. The typical reaction of the process is Reaction (25), in which hydrogen and ammonium sulfate are produced by electrocatalytic oxidation of ammonium sulfite at 80–150 °C and low pressures [135,152]. Ammonium sulfate produced from Reaction (25) reacts with potassium sulfate at about 400–450 °C, producing potassium pyrosulfate in (Reaction (26)), which decomposes to K_2SO_4 and SO_3 at about 790 °C and recirculates to the Reactions (26) and (28), respectively [152,154]. Interestingly, this forms a miscible liquid melt comprised of potassium sulfate and pyrosulfate, which facilitates chemical movements and separations in Reactions (26) and (27). Reaction (28) takes place at high temperatures with the help of a catalyst. The energy required for the process is supplied by a solar system that allows continuous operation. The thermal energy needed to decompose potassium pyrosulfate in a mid-temperature reactor comes from the storage system. The heat of reactants powers the adiabatically operated low-temperature reactor. There is also an energy recovery system that produces electricity required for heating the high-temperature and the operation of electrolytic reactors [152]. A schematic of an electrolytic sulfur-ammonia cycle for hydrogen production is shown in Figure 7.

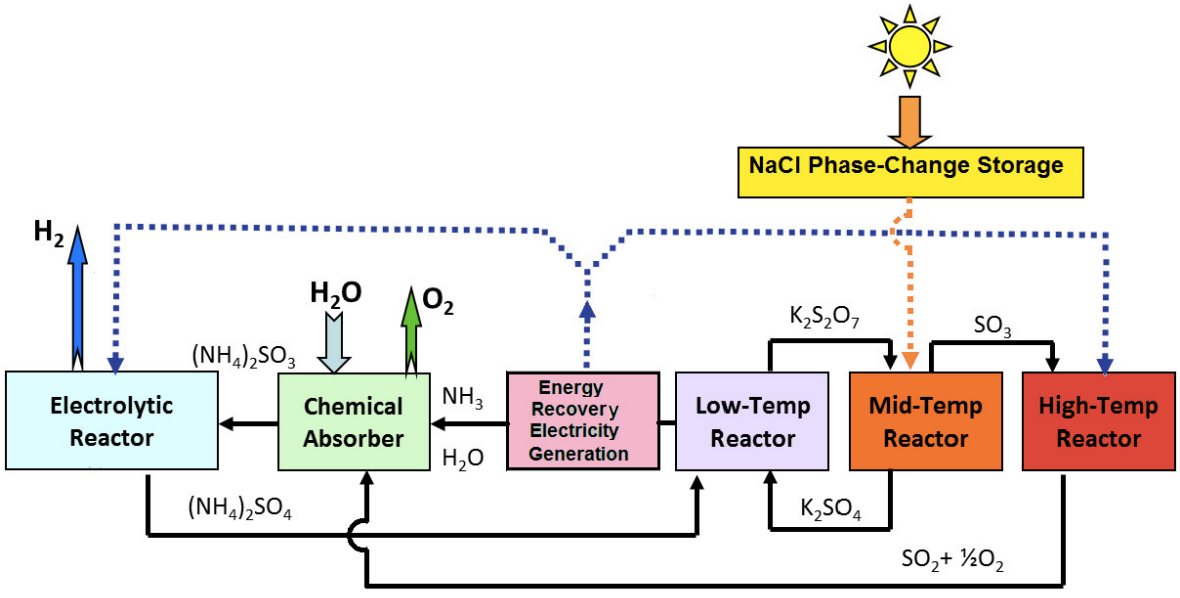

Figure 7. Schematic of an electrolytic sulfur-ammonia cycle [152].

The photolytic sulfur ammonia cycle can also be used with other mediator materials such as zinc oxide. For example, similar steps during hydrogen production in the metal oxide-sulfate sub-cycle. According to Perret et al. [106], the following four steps are the main reactions during this process:

$$SO_2(g) + 2NH_3(g) + H_2O(l) \rightarrow (NH_4)_2SO_3(aq) \ \mathrm{T} = 120\ ^\circ\mathrm{C} \quad (29)$$

$$(NH_4)_2SO_3(aq) + H_2O(l) + hv \rightarrow (NH_4)_2SO_4(aq) + H_2 \ \mathrm{T} = 80\ ^\circ\mathrm{C} \quad (30)$$

$$(NH_4)_2SO_4(s) + ZnO(s) \rightarrow 2NH_3(g) + ZnSO_4(s) + H_2O \ \mathrm{T} = 500\ ^\circ\mathrm{C} \quad (31)$$

$$ZnSO_4(s) \rightarrow SO_2(g) + ZnO(s) + \frac{1}{2}O_2 \ \mathrm{T} = 870\text{–}1000\ ^\circ\mathrm{C} \quad (32)$$

A novel solar hybrid sulfur-ammonia (HySA) water splitting method has been developed by T-Raissi et al. [155], in which ammonia acts as a working agent. Due to the less challenging chemical separation stages, more efficient solar interface, and possibility of thermal storage as an integral part of the process, the HySA cycle is a more efficient water-splitting process. Enabling all-liquid operation and in situ thermal energy storage are the two main advantages of the novel HySA cycle. Energy storage can be either through molten salt storage at the range of 200–300 °C using $K_2S_2O_7/K_2SO_4$ or through thermochemical energy recovery or storage system in the temperature range of 300–500 °C [93].

The photocatalysis process can be carried out in the presence of a 0.5 wt.% Pt/Pd/Ru-doped (or alloyed) CdS photocatalyst. The efficiency of photolysis, defined as the ratio of LHV of hydrogen to the energy of the incident photons with λ = 520 nm, is about 29%. The most important deficiency with this type of hydrogen production is the high cost of noble metal catalysts, which have not yet been resolved. Other challenges include the formation of zinc sulphate and ammonia as a product of the reaction between ammonium sulphate and zinc oxide, transport of zinc sulphate and zinc oxide, coordinated operation of two reactors, etc. [106]. Vagia et al. [93] studied the effect of temperature, catalyst, photocatalyst loading, photoreactor window materials, and light intensity on the hydrogen production yield through the photocatalytic process using CdS and CdS-ZnS core-shell photocatalysts doped by noble metal nanoparticles such as Pt, Pd, and Ru. Many metal hydroxides and metal oxides were generated due to the presence of CdS and ZnS particles (d = 0.5–15 μm) and a trace amount of CdO. The photocatalyst activity of CdS and CdS-ZnS composite was recovered after the depletion of ammonium sulphite. The optimum operating temperature, photocatalyst loading of the solution, ZnS:CdS ratio, co-catalyst loading of CdS, and pH of the system were about 40–60 °C, 0.5–1.0 wt.%, 0.0267, 0.2–1.0 wt.%, and 8, respectively. According to the results, only a 2–2.5 cm suspension layer of the particle effectively took part in photoreactions. Among the photoreactor window materials, including polymer sheets, quartz, and dichroic glass (hot mirror), quartz exhibited the highest hydrogen production rate while the polymer sheets showed the lowest rate. The hot mirror showed 30% lower hydrogen production efficiency than quartz. Shazed et al. [153] simulated the photocatalytic performance of the HySA cycle and reported that the overall solar-to-hydrogen efficiency of the HySA was about 23%.

Corgnale et al. [136] studied the electric input needed for electrochemical oxidation of sulfur dioxide in the HyS cycle. They reported that the electric input was about 20% of the thermochemical stage input. The overall efficiency of the thermochemical cycle has been reported to be in the range of 30–40% based on the hydrogen LHV [156,157]. Bilgen [158] formulated the thermal efficiency process as follows:

$$\eta = \frac{HHV(H_2)}{\sum Q_i} \quad (33)$$

where $\mathrm{HHV}(H_2)$ and $\sum Q_i$ are the higher heating value of hydrogen and the total thermal energy consumption of the process, respectively [134]. In this context, solar-to-fuel efficiency of iron oxide cycle, tin oxide cycle, zinc oxide cycle, cerium oxide cycle, and erbium oxide cycles are about 30%, 29.8%, 29%, 20.2%, and 12%, respectively. Note that the overall efficiency can be increased with increasing heat recuperation. For example, the solar-to-fuel efficiency of the erbium oxide-based cycle can surge from 12% to about 18.86% with 50% heat recovery [159].

Yao et al. [160] improved photocatalyst performance of Pt/CdS catalyst by photochemical treatment in an $(NH_4)_2SO_3$ solution under a vacuum degassed condition followed by photo-radiation exposure (λ = 350–800 nm) for about 20 h. Compared to the conventional Pt/CdS photocatalyst photo-platinized in an aqueous glacial acetic acid solution,

the photocatalytic activity and hydrogen production rate of the photochemically treated Pt/CdS improved about 130 times and 100%, respectively. In addition, Co-doping Pt/CdS photocatalyst with another metal noble or incorporating a transition metal oxide such as Cr_2O_3 can reduce the Pt required and improve the hydrogen production rate [161]. Other CdS-contained compounds such as CdS-TiO_2, CdS-Bi_2WO_6, CdS-ZnO, CdS-g-C_3N_4, CdS-$ZnWO_4$, (CdS + ZnS)/Fe_2O_3, etc. have also improved hydrogen production rate [162–165].

3.1.4. Cu-Cl Cycle

The copper chloride cycle is a multi-step cycle operating at low temperatures with several variations, including two-step, three-step, four-step, and five-step cycles. The nature of the reaction is mainly thermochemical (such as chlorination, oxychlorination, hydrolysis, and thermolysis), electrochemical (such as chlorination and disproportionation), physicochemical (such as complexation), or thermophysical (such as crying) [166]. A schematic illustration of the two-step cycle is shown in Figure 8. The reactions of a sample four-step cycle can be written as follows [103,133]:

$$2CuCl \rightarrow CuCl_2 + Cu \quad (34)$$

$$2CuCl_2 + H_2O \rightarrow CuO.CuCl_2 + 2HCl \quad (35)$$

$$CuO.CuCl_2 \rightarrow 2CuCl + \frac{1}{2}O_2 \quad (36)$$

$$Cu + HCl \rightarrow CuCl + \frac{1}{2}H_2 \quad (37)$$

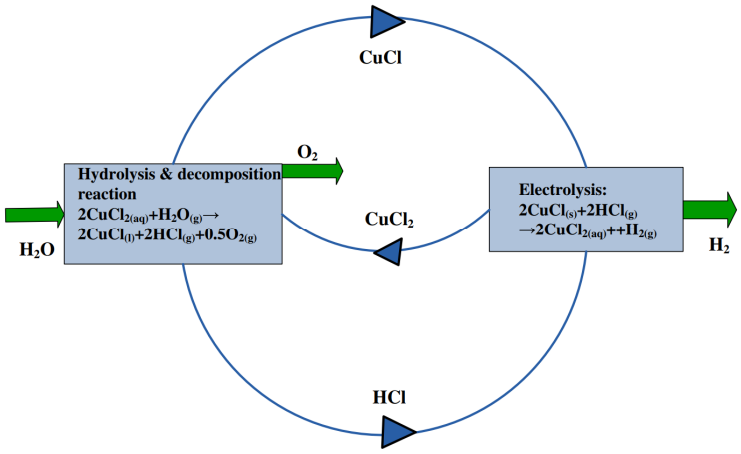

Figure 8. A sample two-step Cu-Cl cycle for hydrogen production (Reproduced with permission from [167], Wiley; 2018).

The first step is an endothermic electrolytic reaction (ΔH = 63 kJ·mol^{-1} H_2 at 25 °C) at temperatures lower than 100 °C (disproportionation process). The second step is composed of an endothermic hydrolysis reaction (ΔH = 117 kJ·mol^{-1} H_2 at 400 °C) at the temperature range of 300–375 °C, and the product is copper oxychloride and HCl gas [133,166,168]. The voltage needed for the electrolysis of CuCl solution at ambient temperature is between 0.4–0.6 V [108]. The third step is an endothermic oxygen production decomposition at 450–530 °C (ΔH = 130 kJ·mol^{-1} H_2 at 500 °C), and the products are molten CuCl and oxygen. The most important issue with this step is decreasing the contact area between the heating medium and reactant particles due to the formation of bubbles (such as oxygen, CuCl vapour, HCl gas, etc.) and their aggregation [133,169]. The fourth step is the exothermic hydrogen generation reaction ($\Delta H = -27.5$ kJ·mol^{-1} H_2 at 25 °C) takes place at 425–450 °C [108,170].

The efficiency of this cycle depends on the ability of electrode materials to produce hydrogen, electrolytic solution, and the performance of each part [133]. The maximum

efficiency of this cycle has been reported to be about 49%, but it decreases over several cycles [103]. In another study, energy and exergy efficiencies of about 21.67% and 19.35% were reported, respectively [171]. The low-temperature reactions offer low-grade waste heat, relatively lower materials costs, and lower voltage needed for the electrochemical step. However, product treatment and separation, as well as corrosive materials, are the most challenging issues with this cycle [108]. Izanloo et al. [168] developed a novel integrated system with high overall efficiency of about 19.6% for simultaneously producing N_2, CH_4, NH_3, O_2, and CO_2. Farsi et al. [172] carried out a comprehensive assessment of the CuCl cycle and concluded that the decomposition temperature of $CuCl_2$ and the amount of excess steam significantly affect the hydrolysis step. Optimizing the temperature of the hydrolysis step can minimize undesirable by-products such as chlorine. Dehydration of $CuCl_2$ can be conducted using spray drying and crystallization of $CuCl_2$. They concluded that this cycle has a promising potential for large-scale hydrogen generation through thermochemical water splitting. Another study conducted an exergo-economic assessment of the cycle and reported that hydrogen production cost is about $3.91 per kg hydrogen for a large-scale plant [173]. More recently, Fan et al. [174] carried out energy, exergy, economic, and the exergo-environmental analysis of the Cu-Cl cycle and reported that energy and exergy efficiencies of the cycle is about 19% and 15%, respectively, and can be improved to 43% and 44% using a cogeneration system consists of an absorption chiller, a gas cycle, a heat recovery steam generator and the copper-chloride cycle which can be used for generating power, cooling, and hydrogen production. They reported that the payback period for this cycle is about 2.5 years. The exergo-environmental analysis revealed that the highest exergy destruction (exergy stability factor) was 0.8 for the Cu-Cl cycle. Another detailed review of the materials and unit operations has been carried out by Naterer et al. [175]. They studied the kinetics of CuCl/HCl electrolysis, electrolysis membrane properties (such as ion-exchange capacity, permeability, conductivity, selectivity, etc.), $CuCl_2$ metastability in H_2O-HCl and its crystallization, materials corrosion in molten copper chloride, corrosion-resistant coatings including metallic (such as Diamalloy 4006) and ceramic (Yttria-Stabilised Zirconia, YSZ) compounds, and system operations (such as cascade heat pumps, Cu-Cl cycle, and heat exchanger for supercritical water-cooled reactor).

A comparative study of some thermochemical cycles conducted by Safari et al. [176] (Figure 9) revealed that the exergy efficiency of V-Cl was higher than the other cycles. In contrast, Cu-Cl and Mg-Cl cycles were more sustainable at operating temperatures. Production costs of the zinc oxide cycle were the highest, mainly due to the high costs of materials, while the sulfur-based category costs less than $2 per kg H_2. Global warming potential (GWP) and hydrogen production costs of the Cu-Cl cycle were about 0.55 kg CO_2.eq per kg H_2 and $2.24 per kg H_2, respectively. Thus, they concluded that the Cu-Cl cycle could be promising for large-scale hydrogen generation through thermochemical water-splitting cycles. The essential advantages of the Cu-Cl cycle are low operating temperature, low costs of materials, ability to improve energy efficiency using low-grade waste heat. At the same time, some significant challenges such as solid handling between processes, corrosive products/by-products, hydrolysis reaction optimization, etc., should be addressed to improve this cycle's overall efficiency further.

3.2. High-Temperature Cycles

Metal oxide cycles are high-temperature two-step thermochemical cycles for hydrogen production through water splitting. These cycles involve fewer and less complex steps while having higher efficiencies [177]. Generally, the main two steps in metal oxide-based thermochemical cycles can be summarized as follows [178]:

$$MO \rightarrow MO_{reduced} + O_2 \ \mathrm{T} > 1000\ ^{\circ}\mathrm{C} \quad (38)$$

$$MO_{reduced} + H_2O \rightarrow MO + H_2 \ \mathrm{T} < \ 1000\ ^{\circ}\mathrm{C} \quad (39)$$

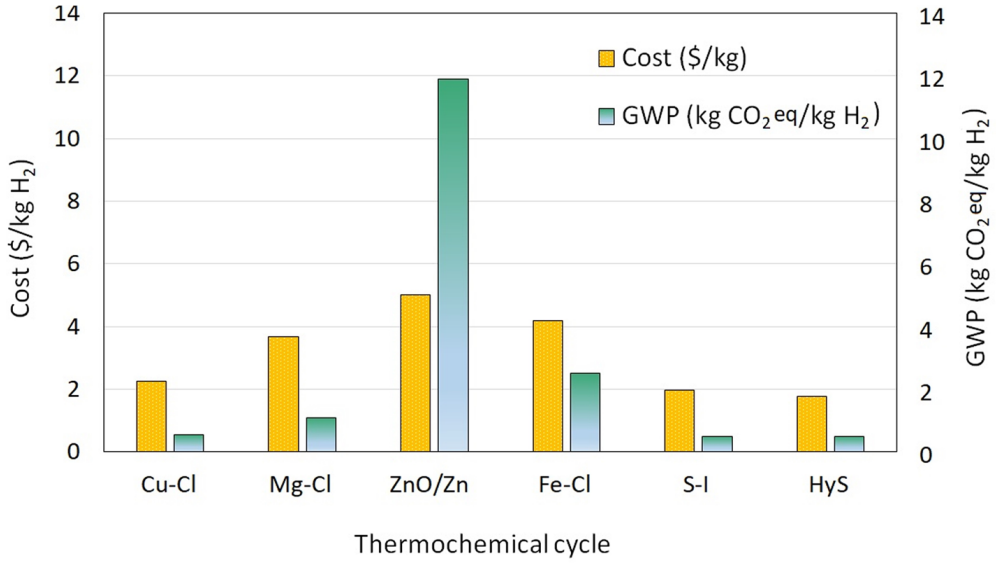

Figure 9. GWP and hydrogen production costs for different thermochemical cycles (Reproduced with permission form [176], Elsevier; 2020).

A number of redox pair cycles such as zinc-based cycles [179], titania-based cycles [180–182], iron-based cycles [183,184], terbium-based cycles [185], manganese-based cycles [186], samarium-based cycles [178,187], etc., have been investigated, but except for some metal oxide cycles, the hydrogen production yield is below 1% [179,188]. Figure 10 shows a sample two-step MO_{ox}/MO_{red} water-splitting cycle schematic. Thermal reduction temperature (T_{TR}) is always significantly higher than the water-splitting temperature (T_{WS}). For example, if the water splitting temperature is about 973 K, the minimum reduction temperature will be about 2173 K. Furthermore, lowering oxygen partial pressure can decrease thermal reduction temperature (Figure 11) [108].

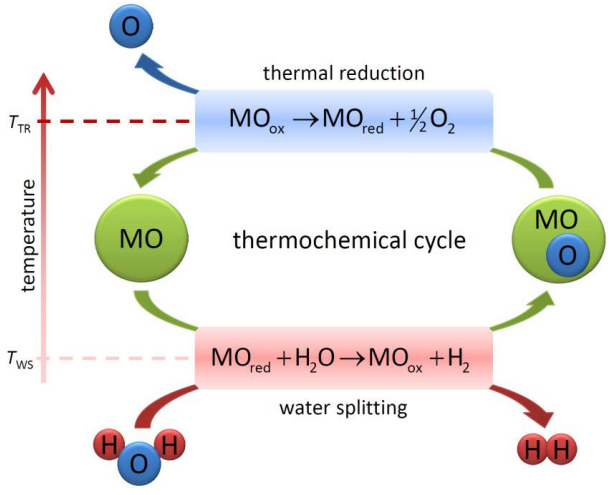

Figure 10. Two-step metal redox system for hydrogen generation [108].

The redox materials should always be in their lower oxidation states which exhibits less noble characteristics than hydrogen. The energetic expenses of the reverse reaction from higher to lower oxidation state (redox material regeneration) should be as low as possible. Thermodynamically, the regeneration reaction should occur at the highest temperature (Figure 12).

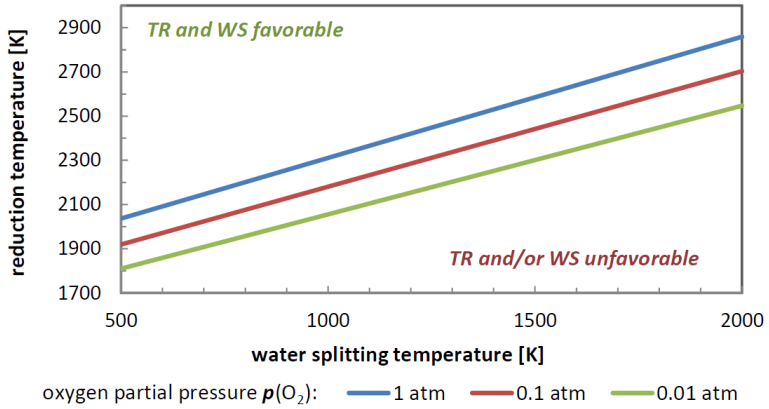

Figure 11. Thermal reduction temperature as a function of oxygen partial pressure [108].

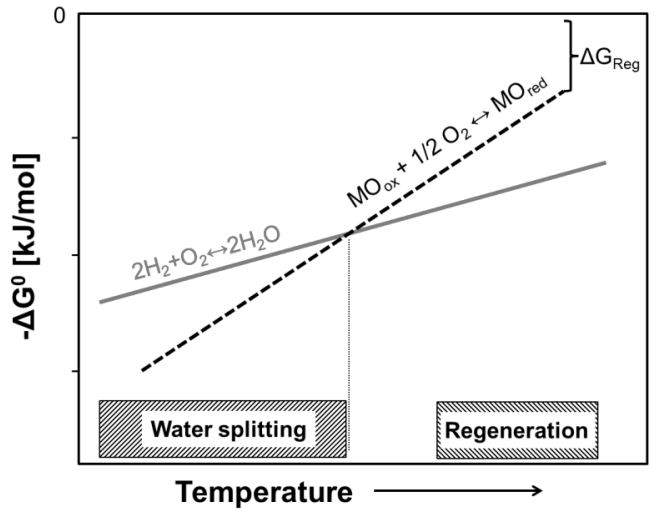

Figure 12. Enthalpy of the $MO_{ox} + \frac{1}{2}O_2 \leftrightarrow MO_{red}$ compared to H_2/H_2O equilibrium [108].

D'Souza [189] summarized the maximum per-pass conversion of water to hydrogen at 600 °C for different metal oxides, and the results are shown in Table 1. Note that the data in this table have been derived at 600 °C to compare the hydrogen production yield at a constant temperature. At the same time, the operating temperature may be higher than 600 °C. Thereby, each cycle's hydrogen production rate is higher. Some of these cycles, along with the other promising thermochemical water-splitting cycles, will be discussed in this section.

Table 1. The highest conversion rate (γ^a) of water to hydrogen per pass at 600 °C [189].

Metal	γ^a (%)	Oxidized Phase
Ni	0.4	NiO
Cd	1.83	CdO
Cu	0	Cu_2O
Co	2.27	CoO
Sn	40.82	SnO_2
MnO	0	Mn_3O_4
Fe	74.79	Fe_3O_4
Fe	74.79	Fe_2O_3

In what follows, a brief discussion on the past and recent progress in some of the metal oxide cycles with the highest hydrogen production yield have been carried out.

3.2.1. ZnO Cycle

Due to the higher efficiency and cost-effectiveness of the ZnO/Zn thermochemical cycle, the zinc oxide cycle arouses great interest. This cycle can be represented by the following equations [190,191]:

$$ZnO \rightarrow Zn + \frac{1}{2}O_2 \quad (40)$$

$$Zn + H_2O \rightarrow ZnO + H_2 \quad (41)$$

The first endothermic step is the thermal dissociation of zinc oxide at about 2000 °C. This step includes the reduction of zinc oxide at high temperatures followed by quenching to oxygen and zinc particles [106,179].

The second reaction is a non-solar water-splitting step in which the recycles zinc from the first step is hydrolyzed, and produces zinc oxide and hydrogen at approximately 425 °C [106,179]. The theoretical maximum efficiency of this cycle is about 39%. Still, the incomplete zinc hydrolysis in the second step, zinc and oxygen recombination in the first step and challenging the heat recovery process of this cycle; significantly lower the overall efficiency [192].

It has been reported that there have been some challenges for further developments of this cycle:

(a) Limited reactor materials capable of enduring the reduction step high temperatures;
(b) Limited efficiency of ZnO decomposition (theoretically about ~70% at 1750 °C);
(c) Challenges with the hydrolysis step due to the formation of zinc oxide on zinc surface area which inhibits further oxidation of the underlying zinc;
(d) Increased costs due to the utilization of a fluid wall reactor to counter particle deposition on reactor walls and loss of zinc metal to condensation;
(e) Low visible-light absorption;
(f) Photo-corrosion of materials [106,191].

Bhosale et al. [193] investigated the effect of ZnO partial reduction as a function of thermal reduction and temperature on the efficiency of the ZnO/Zn cycle. The results showed that the partially reduced ZnO (ZnO-R) performance at 1067 °C was higher than at 967 °C. The highest performance was recorded for the sample with a partial reduction of about 57.2% (R = 57.2%) and operating at 967 °C. Higher ZnO reduction did not significantly enhance the solar-to-fuel energy conversion efficiency and increased only 0.8% when the reduction percentage increased from 57.2% to 100%. However, when 50% heat recuperation (HR) was applied to the cycle operating at 967 °C with R = 57.2%, the solar-to-fuel energy conversion efficiency surged from 57.2% to about 62.6%.

Adequate zinc and oxygen separation can significantly improve the overall efficiency of the cycle. Recent research has focused on rapidly cooling and diluting the gaseous products below the zinc saturation and solidification points [194]. It has been reported that zinc oxidation is a heterogeneous process. If no nucleation sites are available, gaseous zinc and oxygen can coexist in a meta-stable state. The quenching efficiency is affected by the dilution ratio of gaseous zinc in the inert gas flow and the surface temperature on which the products are quenched [179]. A more detailed description of the gaseous zinc and oxygen can be found elsewhere [195]. In situ separation of gaseous zinc and oxygen at high temperatures has also experimentally been an alternative method for zinc and oxygen separation [196]. Wieckert and Steinfeld [197] lowered the reaction temperature of the first step and hindered the recombination using CH_4 or C as reducing agents. Complete ZnO reduction happened at about 1350 °C for ZnO:CH_4 or ZnO:C molar ratio of 0.3 or 0.6, respectively. Müller and Steinfeld [196] investigated the thermal dissociation of zinc oxide in a solar chemical reactor in the temperature range of 1427–1677 °C in a high-flux solar furnace. Quenching the gaseous zinc and oxygen gas was carried out by argon injection and water-cooled walls. The lowest and highest re-oxidation happened halfway in the quench unit (~17%) and the inlet of the quench unit (~80%), respectively. Bhosale [198] also used methane as the reducing agent. According to the results obtained from the

experiments, the reduction of zinc oxide occurred at about 927 °C. It should also be noted that the oxidation possibility of liquid zinc particles is higher than the solid ones [199]. The required solar energy to run the cycle decreased with increasing methane content while increasing methane content increased the solar-to-fuel energy conversion efficiency. A quenching apparatus has also been proposed by Gstoehl et al. [200] to prevent Zn(g) and O_2 recombination. According to the aerosol kinetic model proposed by Alxneit [201], the separation of stoichiometric oxygen gas and gaseous zinc is unaffected by the quench rate, but diluting the mixture before quenching could significantly increase zinc yield. Lindemer et al. [199,202] improved the efficiency of the second cycle step by reducing the proportion of steam and inert carrier gas using a negative axial temperature gradient. Possible complete oxidation of zinc to zinc oxide may occur at a steam-to-zinc ratio greater than 0.5. Xiao et al. [203] deeply investigated the effect of different parameters on the performance of the ZnO-Zn cycle. In this context, Koepf et al. [204] fabricated a small-scale solar reactor plant for zinc oxide reduction. The zinc oxide dissociation of this reactor, which sustained the temperature above 1727 °C and operated for 97 h, was about 28 g/min. The progress in enhancing the performance of the zinc oxide cycle is very promising. This cycle is a promising method for hydrogen generation and has a great potential to improve the efficiency and cost-effectiveness of hydrogen generation.

3.2.2. Tin Oxide Cycle

The tin oxide cycle is a relatively new approach for hydrogen generation through thermochemical water splitting processes. Like zinc oxide, the tin oxide cycle is a volatile metal oxide cycle that requires similar operating temperatures. [205]. The previous tin oxide-based cycle known as the "Soria cycle" or "Sn-Souriau cycle" consisted of three steps [189]:

$$SnO_2 \rightarrow SnO + \frac{1}{2}O_2 \quad (42)$$

$$2SnO \rightarrow SnO_2 + Sn \quad (43)$$

$$Sn + 2H_2O \rightarrow SnO_2 + H_2 \quad (44)$$

This cycle has some significant drawbacks such as low hydrogen yield, impractical separation of metallic tin from tin dioxide by liquefying tin, and slow hydrolysis reaction due to the weak reactivity of tin with water. Thus, a new two-step SnO_2/SnO has been developed [206]:

$$SnO_2 \rightarrow SnO + \frac{1}{2}O_2 \quad (45)$$

$$SnO + H_2O \rightarrow SnO_2 + H_2 \quad (46)$$

The first step is an endothermic solar reduction of SnO_2 to SnO and oxygen (ΔH = 557 kJ·mol^{-1} SnO_2 at 1600 °C), occurring at about 1600 °C. The hydrolysis step involves an exothermic reaction between SnO and H_2O at 450–600 °C ($\Delta H = -49$ kJ·mol^{-1} at 500 °C) to produce tin dioxide and hydrogen [207,208]. Due to the small gap between the reduction temperature (1873 K) and SnO condensation temperature (T_m = 1315 K, T_b = 1800 K), gaseous SnO should rapidly be quenched and condensed as nanoparticles and can be favoured by decreasing oxygen partial pressure [108,206]. Hydrogen yield, hydrogen productivity, intrinsic energy efficiency, and SnO_2-to-SnO conversion of this cycle is about 90%, 14.8 mg_{H_2}/g_{SnO} (or 166.3 mL_{H_2}/g_{SnO}) [96], 42%, and 54% [108], respectively. The exergy efficiency of this cycle is about 29.8% at 1600 °C, which is close to that of the zinc oxide cycle at 2000 °C [96]. Higher solar-to-fuel and cycle efficiencies of about 49.61% and 41.17% can be achieved using 50% heat recuperation [209]. Similar to the zinc oxide cycle, the rate of the hydrolysis step is relatively high in the beginning and gradually levelled off during the process due to the formation and growth of a passivating oxide layer. Thus, a fast reaction-controlled regime followed by a diffusion-controlled regime has been proposed as the reaction mechanism in this cycle [96]. Bhosale et al. [209] carried out a thermodynamic analysis of the SnO_2/SnO cycle and reported that the thermal reduction

temperature can be decreased by reducing the oxygen partial pressure in the carrier gas to about 10^{-3} bar. The results showed that increasing thermal reduction temperature decreased solar-to-fuel and cycle efficiencies. On the contrary, both efficiencies slightly improved with increasing water splitting. The highest solar-to-fuel and cycle efficiencies of this cycle were about 30.08% and 36.26%, respectively, and can be improved to 41.17% and 49.61% with 50% heat recuperation. SnO_2 reduction is affected by the amount of inert gas present in the process and reduction yield decreases with decreasing N_2:SnO_2 ratio [210].

The tin oxide cycle has advantages over the zinc oxide cycle, such as a high dissociation rate of tin dioxide, less dependency on quenching rate due to the higher boiling and melting point of SnO, etc. [205]. Chambon et al. [211] compared the zinc oxide cycle and tin oxide cycle kinetics. The results showed that the hydrolysis step of the zinc oxide cycle was much faster than that of the tin oxide cycle. However, the final hydrogen production of SnO was higher than Zn, which resulted in similar hydrogen production at the end of both cycles (about 6 mmol hydrogen per gram of zinc oxide or tin dioxide). Implementing an empirical depletion model, they determined the kinetic parameters for an uncoupled Arrhenius equation. The activation energy and reaction order for the hydrolysis step of ZnO were about 87 kJ·mol^{-1} and n = 3.5, respectively, while the same values for SnO were about 122 kJ·mol^{-1} and n = 2, respectively. These results were validated using a model-free method at different heating rates. Despite several advantages of the tin oxide cycle, low exothermic heat at 500 °C leads to a weak self-heating and promotes the reaction rate and low-temperature back reaction, which increases the time needed for completing the cycle. These challenges can be addressed using optimal partial pressure and steam feeding before reaching the maximum operating temperature (~600 °C) [212]. Altogether, this cycle can be considered a promising cycle for hydrogen production, and further developments can improve its cost-effectiveness and performance.

3.2.3. Iron Oxide Cycle

While ZnO/Zn and SnO_2/SnO cycles are known as volatile redox pairs, Fe_3O_4/FeO, CeO_2, $CeO_{2-\delta}$, perovskites, and ferrites are known as non-volatile redox pairs for hydrogen generation. Iron oxide (Fe_3O_4/FeO) water splitting thermochemical cycle, which was first discovered by Nakamura [213], is another two-step hydrogen generation process based on the reduction and oxidation of iron ions (Fe^{3+} and Fe^{2+}). Non-volatile iron oxide water splitting cycle benefits from the continuous release and removal of oxygen during the solar reduction step. This cycle avoids the recombination reaction with oxygen and involves non-corrosive materials [96]. The main two steps of iron oxide redox pair can be written as follows [96,188]:

$$Fe_3O_4(s-l) \rightarrow 3FeO(s-l) + \frac{1}{2}O_2 \quad (47)$$

$$3FeO(s) + H_2O(g) \rightarrow Fe_3O_4(s) + H_2 \quad (48)$$

The first step is a highly endothermic solar reduction reaction ($\Delta H^\circ = 319.5$ kJ·mol^{-1}) of magnetite, which happens at high temperatures (T > 2200 °C) below the atmospheric pressure. The reduction step takes place at a temperature higher than the melting point of magnetite (1597 °C). The high temperature required for this step results in materials vaporization during the process, decreasing the surface area, and rapid materials deactivation in cyclic reaction [96,108,214]. On the other hand, the second step is a low-temperature wustite (FeO) hydrolysis (T < 1300 °C) which involves an exothermic reaction ($\Delta H^\circ = -33.6$ kJ·mol^{-1}) [96,108,177]. As depicted in Figure 13, the most favourable theoretical hydrolysis temperature of FeO is below 800 °C, and the conversion rate of FeO decreases with increasing temperature [96]. Product separation can be achieved using a counter-current flow with a gas outlet opposite of the solid outlet in a solar reactor [215]. The maximum theoretical efficiency of the Fe_3O_4/FeO according to the reactions temperatures and HHV of hydrogen (286 kJ·mol^{-1}) is about 37.1% [96], while the real solar-to-hydrogen efficiency of the Fe_3O_4/FeO cycle is about 18% [216]. Due to the formation of a passive oxide layer, the maximum chemical conversion of direct hydrolysis is about 75% [215].

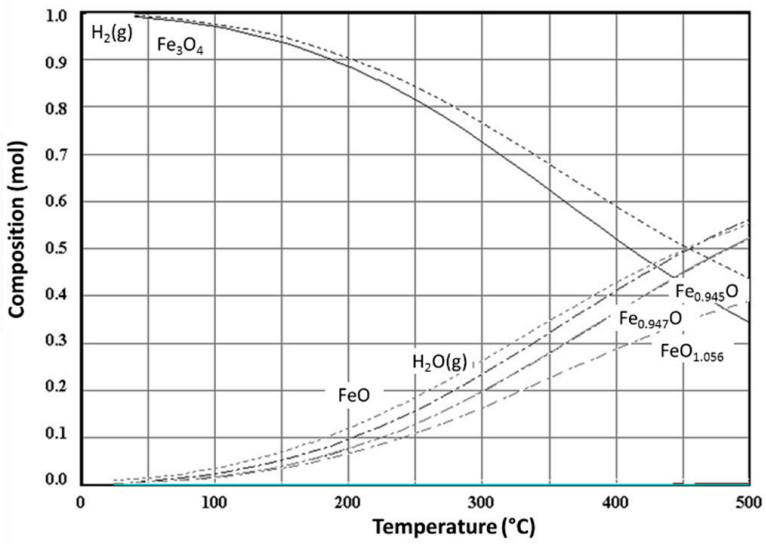

Figure 13. The theoretical conversion rate of wustite in the thermodynamic equilibrium of Fe-O-H system with 3 mol FeO and 1 mol H_2O, and $P(N_2)$ = 1 bar [96].

According to the results of the thermodynamic evaluation carried out by Charvin et al. [188], a non-stoichiometric wustite phase ($Fe_{1-y}O$) may form during the process. Stoichiometric wustite presents more Fe^{2+} for hydrogen production, but non-stoichiometric wustite exhibited higher reaction rates, probably due to the higher defect densities, serving as magnetite nucleation sites. Lowering the total pressure decreased the required temperature needed for the process and thus improved the exergy efficiency due to the lower radiation losses (αT^4). Hydrogen yield increased with increasing operating temperature, especially at the beginning of the process. Due to the formation of a passive layer (Fe_3O_4) at the surface of the particles, the reaction rate decreases with time. This indicates the importance of the exposure of fresh non-oxidized layers to the steam. They have also reported that the diffusion inside the porous outside layer of Fe_3O_4 is a key factor in determining the performance of the cycle, and more than 90% of the evolved hydrogen was generated during the first 3 min. Small particle size (~50 μ) improves the cycle performance by: (a) complete oxidation due to the high surface-to-volume ratio, (b) increasing the surface area and reaction kinetics, mass transfer, and heat transfer, and (c) enabling particle fluidization or continuous reactant feeding and particle removal due to their possible entrainment in gas flow [188]. Thermodynamics, mass/energy balance, reaction kinetics, etc., of the Fe_3O_4/FeO cycle have been thoroughly discussed by Xu et al. [216]. On the whole, this cycle is a low-cost thermochemical water splitting method for hydrogen production that uses abundant chemical materials and has a promising potential for large-scale hydrogen generation.

3.2.4. Ferrite Cycle

Lowering the reduction temperature can benefit the process by lowering the capital costs and hindering materials vaporization. Therefore, several researchers have focused on lowering the temperature needed to reduce the oxide and proposed mixed solid solutions of mixed-metal oxides (ferrites) such as Fe_3O_4/FeO and M_3O_4/MO (M = Zn, Co, Ni, Mn, etc.) with spinel crystal structure [108,177,188]. These cycles are known as "ferrite cycles," which can lower the initial temperature (~2230 °C) down to 1340–1500 °C [186,203]. The following reactions take place during this process (M = Ni, Co, etc.) [217]:

$$MFe_2O_4 \rightarrow (MO + 2FeO)_{ss} + \frac{1}{2}O_2 \quad (49)$$

$$(MO + 2FeO)_{ss} + H_2O \rightarrow MFe_2O_4 + H_2 \quad (50)$$

It should be noted that the cell parameter of the reduced phase and MO is close to each other. Thus, the following reaction may happen [217]:

$$3MFe_2O_4 \rightarrow 3MO + 2Fe_3O_4 + \frac{1}{2}O_2 \quad (51)$$

The most promising mixed oxide cycles for hydrogen production with high hydrogen yield and cyclability are nickel ferrite ($NiFe_2O_4$) and cobalt ferrite ($CoFe_2O_4$) [203,217,218].

It has been reported that supporting ferrite over ZrO_2 can simultaneously lower the temperature and enhance energy radiation absorption in the solar setup [186]. Furthermore, thermal stresses of the redox material during the thermochemical cycles can intensify grain growth and decrease the specific surface area and pore volume. Thus, the rate of hydrogen generation may decrease during the cycles. Therefore, ceramic nanoparticles such as zirconia, yttria, and YSZ can reduce grain growth and slightly increase hydrogen generation [219]. Dispersion of ferrite in zirconia improves reactivity and enhances the kinetics of reduction and hydrolysis steps. Fe_3O_4/m-ZrO_2 has high hydrogen productivity and a high conversion rate of Fe_3O_4 to FeO of about 60% at 1600 °C without m-ZrO_2 to t-ZrO_2 phase transition [220]. Zirconia supports can hinder iron oxide coagulation and alleviate the high-temperature sintering. Thus higher activity and activity retention can be achieved compared to the unsupported ones [218]. $Co_xFe_{3-x}O_4$/m-ZrO_2 with x = 0.4–0.7 showed high reactivity for hydrogen production at 1400 °C under inert atmosphere [221]. $Ni_xFe_{3-x}O_4$/m-ZrO_2 have also high reactivity when the value x reached x = 1.0 [214]. Reñones et al. [222] studied the ferrite conversion and hydrogen production of nickel ferrite supported on calcium-stabilized zirconia and reported an enhanced hydrogen generation efficiency due to the promoted high active phase dispersion caused by the formation of calcium zirconate, which acted as a physical barrier and hindered sintering. Fernández-Saavedra et al. [223] examined the hydrogen production and kinetic parameters of commercial nickel ferrites. The results showed that the Ni ferrite cycle's hydrolysis reaction and activation reaction could fit a second-order reaction and two-dimensional diffusion models, respectively. The calculated activation energies for the activation and hydrolysis reactions were about 261.65 kJ·mol^{-1} and 34.53 kJ·mol^{-1}, respectively. The nickel ferrite cycle generated about 0.5 mmol(H_2)·g^{-1} per cycle.

The overall conversion efficiency of the first step and oxidation rate in the second step in the ferrite cycle is not high enough. Thus, co-precipitating and implementing deposition techniques have been proposed to improve overall performance [106,203]. Teknetzi et al. [218] used zirconia and sacrificial plates (carbon black and polyethylene glycol) to enhance the thermal stability of the nickel ferrite samples. The highest thermal stability was recorded for the sample containing 20 wt.% carbon black and 10–30 wt.% zirconia. Higher carbon black and zirconia contents decreased the mechanical strength and porosity, respectively. The samples with the optimum distribution of pore size and the highest porosity exhibited the highest performance. Encapsulating nickel ferrite particles in a ceramic material can further mitigate grain growth and hinder sintering at high temperatures. Amar et al. [219] synthesized core-shell $NiFe_2O_4/Y_2O_3$ nanoparticles via the sol-gel method and reported a relatively stable hydrogen generation over multiple cycles. The shell thickness and the d-spacing were about 3.26 nm and 0.48 nm, respectively. The hydrogen volume generated in the first and fifth cycles and average hydrogen volume of the core-shell nanoparticles were approximately 10.39 mL·g^{-1} and 8.7 mL·g^{-1}, respectively. In comparison, the same data obtained for the powder mixture were about 13.07 mL·g^{-1} and 3.25 mL·g^{-1}, respectively. According to the results, the hydrogen volume was stable in the case of core-shell nanoparticles. Still, the hydrogen generation rate of core-shell nanoparticles was lower than that of $NiFe_2O_4/Y_2O_3$ powder mixture, probably due to the diffusional limitations associated with the core-shell nanoparticles and the lesser grain growth for the core-shell nanoparticles compared to the power mixture of $NiFe_2O_4/Y_2O_3$.

Scheffe et al. [224] deposited Co-ferrites on alumina substrate through atomic layer deposition (ALD) technique. Due to the reaction between alumina and Co-ferrite at low temperatures (200–300 °C), the hercynite phase ($FeAl_2O_4$) was formed during the process.

Due to this reaction, alumina substrate is unfavourable because it deactivates the ferrite phase; however, ferrites can be reduced at lower temperatures in the presence of an alumina substrate. The results confirmed that water splitting started at about 1000 °C, and a large amount of hydrogen was generated at about 1200 °C when hercynite was formed, while little or no hydrogen was generated at 1400 °C using Co-ferrite coated on zirconia.

Goikoetxea et al. [217] compared the hydrogen generation efficiency of Co ferrite and Ni ferrite thermochemical cycles. XRD results showed that due to the partial reduction of spinel ferrites, a new wustite phase with a general formula of $M_{1-x}Fe_xO$ (M = Co or Ni) was formed during the activation process. Both ferrites have homogeneous distribution. However, only Ni ferrite exhibited a total recovery of the original spinel phase, and Co ferrite was enriched by the wustite phase, which hindered the full recovery of the original spinel phase during the thermochemical cycle. Thereby, although the hydrogen production yield of Co ferrite was higher than that of Ni ferrite in the first cycles, the hydrogen production yield of Co ferrite decreased as previously discussed. Other ferrites, such as Mn-ferrites, Zn-ferrites, etc., showed lower performance than the compounds mentioned above [108]. Ferrite cycles can produce large amounts of hydrogen, and depositing thin films of ferrites on supports can hinder the sintering and enhance the performance. Numerous ferrite compounds have been investigated so far. However, Ni-ferrites and Co-ferrites with zirconia support are the most suitable compounds for hydrogen generation through water-splitting thermochemical cycles.

3.2.5. Manganese Oxide Cycles

Manganese oxide cycle is a three-step thermochemical water splitting method that consists of three main reactions:

$$Mn_2O_3 \rightarrow 2MnO + \frac{1}{2}O_2 \quad (52)$$

$$2MnO + 2NaOH \rightarrow 2\alpha - NaMnO_2 \quad (53)$$

$$2\alpha - NaMnO_2 + H_2O \rightarrow Mn_2O_3 + 2NaOH \quad (54)$$

The first step is the reduction of Mn_2O_3 to MnO at about 1873 K, the second step is the oxidation of Mn^{2+} to Mn^{3+} as α-$NaMnO_2$ and hydrogen evolution from the reaction between MnO and NaOH at about 973 K, and the final step is the formation of Mn_2O_3 and NaOH from the reaction between H_2O and α-$NaMnO_2$ at about 100 °C [225]. Marugán et al. [226] carried out a thermodynamic assessment of the Mn_2O_3/MnO cycle. They concluded that the hydrogen production step starts at 50 °C and completes at 150 °C at the total pressure of 1 bar and N_2/MnO ratio of 1. The temperature required to complete the reaction increases with increasing the total pressure of the system. On the other hand, the higher the N_2/MnO ratio, the lower the temperature needed for completing the reaction.

It should be noted that three phases are present in the phase diagram of Na-Mn-O in the temperature range of 650–850 °C, namely α-$NaMnO_2$, β-$Na_{0.7}MnO_2$, and α-$Na_{0.7}MnO_{2.05}$. Amongst these phases, only α-$NaMnO_2$ can be hydrolyzed in water to recover Mn_2O_3. Thus, the structure of the mixed oxides can have an immense influence on the performance of the cycle [227,228]. The highest efficiency of this cycle with and without heat recovery is about 74% and 16–22%, respectively [229]. It has also been reported that when oxygen concentration exceeds a critical point (0.25%), the recombination reaction is the dominant process, and the only way to obtain higher conversion efficiency is by elevating operating temperature.

On the other hand, gas flow rate and temperature control the dissociation process when the oxygen concentration is below the critical point. The results showed that a higher conversion rate could be achieved using an inert atmosphere and a rapid quench [230]. Hydrogen formation can be promoted using a vacuum environment; however, the combined effect of low pressure and high temperature can evaporate 30% of Na during the process [231].

Kreider et al. [225] improved the hydrolysis of α-$NaMnO_2$ and recovery of Mn^{3+} by modifying the manganese oxide cycle. The hydrolysis step requires a large amount of water to remove Na and recover NaOH. Using Fe with the mixed oxide, surged NaOH recovery from 10% to 35% in the hydrolysis step at NaOH concentration above 1M. The highest conversion rate of the third cycle was about 65%. It is interesting to note that the excess water reduces the thermal efficiency of the cycle. Thereby, the addition of a secondary metal such as zinc, iron, or cobalt has shown promising results in improving the hydrolysis step's performance and reducing the amount of water needed for the cycle by a factor of three [98]. In this context, Orfila et al. [232] fabricated $Mn_{3-x}Co_xO_4$ mixed oxides ($0.9 < x < 2.7$) and reported that the metal oxide reduction occurred in the temperature range of 1048–1164 K, which is much lower than the temperature needed for the Mn_2O_3/MnO oxides (1723 K). The operating temperature decreased using a higher inert gas flow. The $Mn_{2.1}Co_{0.9}O_4$ sample showed the lowest operating temperature and the highest solar-to-fuel and exergy efficiencies among all of the samples. The optimum temperature for the oxidation step was about 1165–1325 K. Furthermore, the secondary metal can hinder the formation of sodium/manganese birnessite. On the one hand, if this phase does not decompose, it can accumulate and prevent the cycle from being closed. On the other hand, decomposition of this phase can reduce the efficiency of the cycle [106].

Bayón et al. [231] studied the effect of morphology and structural characteristics on the performance of the manganese oxide cycle. They used four types of MnO: (a) commercial MnO (Sigma Aldrich, St. Louis, MO, USA, 99%) (C-MnO), (b) commercial MnO mechanically milled for 30 min (M-30-MnO), (c) commercial MnO milled for 10 min (M10-MnO), and (d) synthesized MnO from Mn_3O_4 (S-MnO). The results showed that decreasing the particle size favoured contact with NaOH and improved hydrogen production. In addition, the highest conversion rate of about 83% was recorded for the S-MnO sample. Mn_3O_4-Na_2CO_3 [233], MnO-Na_2CO_3 [234], Mn_3O_4-NaOH [235], sodium manganese ferrite [236] are other multi-step manganese oxide-based thermochemical water-splitting cycles that have also been investigated as potential hydrogen production methods. A schematic representation of a four-step manganese-based thermochemical water splitting cycle is shown in Figure 14. Note that, as defined before, this cycle is considered a low-temperature cycle according to the operating temperatures specified in the table below the figure [233]. Altogether, the main advantages of this cycle are its high thermal efficiency, abundance and non-hazardous reactants [106]. In contrast, the main drawbacks are the high conversion temperature of Mn_2O_3-to-MnO, volatility of sodium hydroxide at above 800 °C, loss of Na, poor crystallinity, and large particle size [229,231].

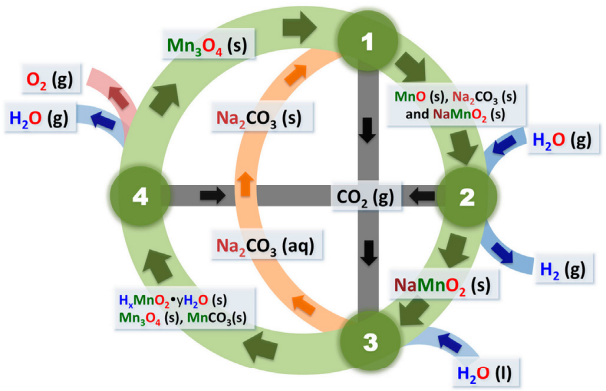

Step	Reaction	Temp (°C)
1	$3Na_2CO_3(s) + 2Mn_3O_4(s) \rightarrow 4NaMnO_2(s) + 2CO_2(g) + 2MnO(s) + Na_2CO_3$	850
2	$2MnO(s) + Na_2CO_3(s) + H_2O(g) \rightarrow H_2(g) + CO_2(g) + 2NaMnO_2(s)$	850
3	$6NaMnO_2(s) + ayH_2O(l) + (3+b)CO_2(g) \rightarrow 3Na_2CO_3(aq) + aH_xMnO_2{\bullet}yH_2O(s) + bMnCO_3(s) + cMn_3O_4(s)$	80
4	$aH_xMnO_2{\bullet}yH_2O(s) + bMnCO_3 + \rightarrow (2-c)Mn_3O_4(s) + ayH_2O(g) + bCO_2(g) + 0.5O_2(g)$	850
Net	$H_2O(g) \rightarrow H_2(g) + 0.5O_2(g)$	

a, *b* and *c* satisfy following relations: $a + b + 3c = 6$ and $(4-x)a + 2b + 8c = 18$

Figure 14. A sample representation of manganese oxide-based thermochemical water splitting cycle for hydrogen generation [233].

3.2.6. Other Metal Oxide Cycles

Ceria-based oxide cycle is a two-step water splitting technique in which the products of the first step at about 2000 °C are non-stoichiometric ceria and oxygen. In the second step, the non-stoichiometric ceria rapidly reacts with water vapour and produces hydrogen and stable ceria [210]. Hydrogen generation and reduction efficiencies can be improved using dopants and additives such as Al, Mn, Fe, Co, Zn, or Zr [237]. For example, 50% zirconia addition can result in a 70% reduction yield at 1500 °C. $Ce_{0.75}Zr_{0.25}O_{2-\delta}$ can be reduced at a low temperature of about 1500 °C [238]. However, the low solar-to-fuel efficiency of this cycle compared to the other cycles such as zinc oxide or tin oxide is the main disadvantage of this cycle. The two-step erbium oxide cycle (Er_2O_3/ErO) has also been investigated as a potential thermochemical water splitting route. Still, the efficiency of this cycle has been reported to be much lower than the other cycles [159]. Samarium oxide cycle is another thermochemical water splitting method with slightly higher efficiency than Er oxide, but the efficiency is still low (~31% with 50% heat recuperation) [187]. Barium oxide cycle (BaO/Ba) has recently been studied and reported that the operating temperature can be lowered using some additives such as CuO, MnO_2, or Fe_2O_3, or by applying a vacuum condition or reducing oxygen partial pressure. However, its efficiency, energy density, reversibility are not high enough [210]. The cadmium oxide cycle is a high-temperature two-step volatile metal oxide cycle.

The first step involves decomposition of CdO to gaseous Cd and oxygen at about 1450 °C, and the next step is the hydrolysis reaction between Cd and H_2O to produce CdO and hydrogen at about 450 °C [106]. The hybrid cadmium cycle is a cadmium oxide-based cycle in which the second step of the conventional cadmium oxide cycle is divided into two reactions: (a) formation of $Cd(OH)_2$ and hydrogen from the reaction between Cd and H_2O, and (b) formation of CdO and H_2O at about 375 °C [98,189]. Cadmium carbonate is another cadmium oxide-based cycle which consists of three steps, namely decomposition of CdO to Cd and oxygen at 1450–1500 °C, the reaction between Cd, H_2O, and CO_2 at 350 °C to produce $CdCO_3$ and H_2, and decomposition of $CdCO_3$ to CO_2 and CdO at 500 °C [98]. It has been reported that rapidly quenching the decomposition product is necessary because gaseous Cd can rapidly recombine with oxygen after CdO dissociation and reduce cycle efficiency and cadmium yield. Mixing CdO with ZrO_2 can hinder this recombination due to the dispersion of cadmium metal in the zirconia matrix [106,189]. The hydrogen production capacity of binary oxide systems such as Ni-Mg-O and Co-Mg-O have also been investigated. It has been reported that an appropriate composition of the oxides enhances the reduction degree in these systems. The uniform incorporation of cobalt oxide particles into the magnesium oxide structure in the Co-Mg-O oxide system may result in a strong chemical interaction between the two oxides. MgO matrix protects the cobalt oxide species from agglomeration and migration at high operating temperatures. Thereby, the Co-Mg-O system has stable and reproducible performance in cyclic reduction/reoxidation reactions in the hydrogen production industry [239]. Ni-Mg-O is another binary system where nickel oxide species are uniformly distributed within the magnesium oxide matrix. Partial substitution of magnesium ions with nickel ions can result from a solid solution during the process, and the prominent hydrogen uptake occurs at about 350–550 °C [240]. Overall, among the metal-oxide cycles, Zn/ZnO and FeO/Fe_3O_4 thermochemical cycles represent higher hydrogen production and can be used as a new research direction. Other cycles such as SnO_2/SnO, CeO_2/Ce_2O_3, perovskite, GeO_2/GeO, MgO/Mg, CdO/Cd, Mn_2O_3/MnO, etc. suffer from the low recovery of the reduced materials, low solar-to-fuel efficiency, difficulties with handling the reduced product, low hydrogen yield, high operating temperature, high operating costs, high heat capacity, toxicity of the materials, etc. [106,178,203,241,242].

It should also be noted that microstructure stability, atomic mobility, the surface of the redox material, and solid-state transformation play essential roles in determining the performance and efficiency of the cycle. Reconstructive transformation can form significant nucleation barriers and decrease the overall efficiency [108,243]. If the nucleation

density of the new phase is not high enough, significant coarsening will go along with the phase transformation. The change in oxidation state within a parent structure can benefit nucleation in certain multi-valent metal oxides. Nonstoichiometric defect structures offer high oxygen diffusion, promoting redox reaction from the surface to the bulk of the compound [108]. High atomic mobility can cause rapid sintering and coarsening. The high surface area has an immense influence on promoting the solid/gas redox reaction, and small particle size with a high surface area is mandatory. Particle and crystal growth can be hindered by lowering the grain boundary mobility by segregating solutes in grain boundary precipitates or zones [243–245]. Using the redox material as a coating on a stable substrate can also be beneficial [108]. Doping metal oxide systems with a specific dopant can reduce the operating temperature and improve cycle stability, reducing the hydrogen yield. Composite systems can further reduce the operating temperature and improve hydrogen production [210].

4. Summary

Optimal energy strategy plays an essential role in improving process optimization to increase lifetime and cost-effectiveness. Energy and exergy analysis of an S-I cycle coupled with HI-I_2-H_2O electrolysis has been conducted by Ying et al. [110]. The whole cycle was divided into three sections, i.e., Bunsen reaction, sulfuric acid decomposition, and HI-I_2-H_2O electrolysis. According to the results, the energy and exergy efficiencies of the system were about 15.3–31.0% and 32.8%, respectively. Due to the transformation of electricity to exergy in an electrolytic cell, sulfuric acid decomposer and condenser and Bunsen reaction sections accounted for about 93.0% and 63.4% of the exergy destruction, respectively. The highest exergy efficiency of the proposed S-I cycle was about 32.8% which was lower than the four-step Cu-Cl cycle (75.7% [246]) and Zn/ZnO cycle (~40%) [247]. The highest energy efficiency was also about 31.0%, which was lower than the Cu-Cl (41.9% [246]) and Zn/ZnO cycles (~40% [192]), implying that more studies should be conducted to improve the overall energy and exergy efficiencies of the proposed cycle such as appropriate waste heat recovery and internal heat exchange was recommended by the authors.

Juárez-Martínez et al. [91] optimized the energy efficiency of an S-I cycle using a new network consisting of four heat exchangers and a heuristic-ruled method. The effect of the new network of heat exchangers on the system's efficiency was analyzed, and it was found that the energy needed for cooling decreased. Thus, the overall thermal energy efficiency improved by about 10%.

Wang et al. [248] analyzed the energy efficiency of direct solar hydrogen using low-cost materials. As the current hydrogen production systems suffer from either low efficiencies or expensive materials, they claimed that their proposed hydrogen generation system comprised of catalysts and low-cost light-absorbers could reach 20% efficiency of solar-to-hydrogen (STH) conversion by coupling high-performance perovskite-Si tandem cells with earth-abundant catalysts. The electrodes were made of high-density NiMo with flower-stem morphology with minimal reaction overpotential (~6 mV at 10 $mA \cdot cm^{-2}$) and increased reaction sites. Enhancing the performance of perovskite cells with an open-circuit voltage of 1.271 V can improve surface passivation and, consequently, surge the overall efficiency from 20% to 25%. In another attempt, Jia et al. [249] reported a higher hydrogen efficiency of over 30% using photovoltaic-electrolysis technology for water splitting. The system includes an InGaP/GaAs/GaInNAsSb triple-junction solar cell in series with two polymeric electrolyte membrane electrolyzers. Since the mentioned assembly produced a high voltage to drive the electrolyzers, no extra input power was used in the system. The operating capacity of the electrolyzers was well matched to the maximum output power of the photovoltaic cell by adjusting the solar concentration. A schematic of the PV-electrolysis is shown in Figure 15. High STH efficiency of about 30% was reported for the PV-electrolysis system. It is interesting to note that using two electrolyzers in series with a high-efficiency solar cell minimized the required additional voltage, thus improving the water splitting efficiency.

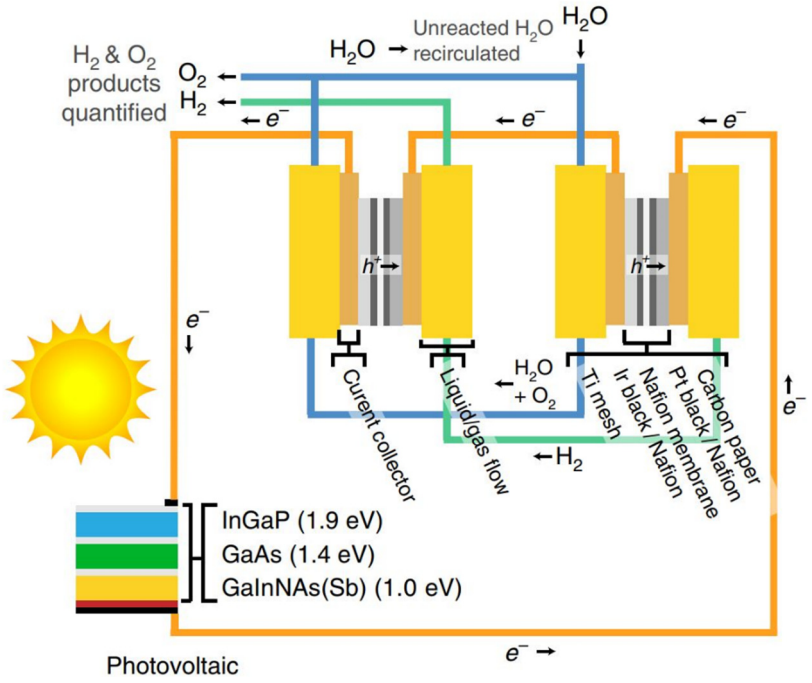

Figure 15. Schematic of PV-electrolysis system for hydrogen production [249].

According to the techno-economic assessments in 2009, the cost of hydrogen production using the HyS process with nuclear reactor is \$5.34–6.18 per kg [250]. On the other hand, the costs of solar-driven hydrogen production are approximately in the range of \$2.64–7.58 per kg depending on the solar plant efficiency, heliostat cost, location, thermochemical efficiency, etc. [136,251,252]. It has been reported that the sulfur dioxide depolarized electrolyzer (SDE) can significantly reduce the costs and electrical power required for the process [134]. It should also be noted that the realistic thermochemical efficiency of the S-I cycle is in the range of 35–38% based on hydrogen LHV, and costs of hydrogen production with an S-I cycle equipped with a nuclear reactor is in the range of \$3.50–12.0 per kg [253,254]. As listed in Table 2, D'Souza [189] estimated the overall cost of hydrogen production (per kg hydrogen) in different cycles in 2015 and 2025. US DOE chose these technologies in collaboration with the TIAX laboratory as the most promising thermochemical water-splitting cycles. As has been established by the US DOE, hydrogen production costs should be in the range of \$6 and \$2–3 per kg H_2 in 2015 and 2025, respectively. As can be seen in this table, the ferrite cycle (Ni ferrite thin film) shows great potential for hydrogen production, followed by the HyS cycle. However, further developments are required to satisfy the long-term stability and efficiency of these cycles to decrease capital expenditures (CAPEX) and operating expenses (OPEX).

Table 2. Hydrogen production costs (\$ per kg H_2) of different thermochemical water splitting cycles [189].

Years	HyS	CuCl	Ferrite	SA	ZnO	MnO	S-I
2015	5.68	6.83	4.06	7.78	6.07	-	-
2025	3.85	5.39	2.42	4.71	4.18	4.63	4.68

Hydrogen production through thermochemical water-splitting cycles is a clean and attractive method for addressing the global hydrogen energy demand. Currently, the most common methods for hydrogen generation are fossil-based technologies, and they result in air pollution and greenhouse gas emissions, resulting in global warming. Clean hydrogen can be produced using thermochemical cycles, but these cycles need to be studied to improve efficiency and lower the overall operation costs. A number of the recent studies and their significant findings has been summarised in Table 3. As listed in this table,

each technology has weaknesses and strengths compared to the other ones. Overall, it is suggested that future studies should focus on improving the overall efficiency of the cycles, especially the Cu-Cl low-temperature cycle as well as zinc oxide and ferrite high-temperature cycles, by using the most cost-effective catalysts, optimizing structural and microstructural properties, removing impurities from the cycles, promoting the redox reactions and conversion rates, doping, handling the byproducts, etc. Since catalysts can enhance reaction rates and help improve the hydrogen yield, a cost-effective catalyst selection will be helpful. Nanomaterials can also improve the efficiency of the cycles, but their weaknesses, such as agglomeration, grain growth, and costs, should be addressed efficiently. Non-stoichiometry can facilitate the reactions and promote hydrogen production in metal oxide cycles. The potent combination between the thermodynamics and kinetic properties of the reactions and the structural/microstructural properties of the materials such as structure, morphology, composition, etc. and possible new synthesis routes should be considered in the subsequent studies to improve the cost-effectiveness of the cycles further. Implementing simulations for predicting the results of using new materials, new synthesis conditions, rate of reactions in each step, etc., can be beneficial.

Table 3. Summary of the significant discoveries of some of the essential thermochemical water-splitting cycles.

Cycle	Major Discovery	Ref.
S-I	Optimization of the Bunsen section for liquid–liquid separation. Increasing iodine content improved separation characteristics. The optimum I_2/H_2SO_4 ratio was in the range of 2.45–3.99 at 70–85 °C	[107]
S-I	Developed a microporous membrane resistant to sulfur trioxide composed of α-alumina support, ZrO_2-SiO_2 intermediate layer, and organosilica sol top layer. High Si:Zr ratio and large pore of the ZrO_2-SiO_2 showed higher O_2/SO_3 selectivity and higher chemical stability against SO_3	[115]
S-I	Developed a modified cycle with fewer steps and used a steam boiler. The modified cycle has a higher HI decomposition rate, and the Bunsen reaction happened at lower temperatures.	[116]
S-I	Catalysts with hierarchical pore structure and higher specific surface area and micropore proportion of about 50% showed higher catalytic activity.	[117]
S-I	N doping promotes HI decomposition rate	[102]
HyS	Increasing Fe content in Fe/Al and Fe/Ti binary metal oxide catalysts improved catalytic activity	[143]
HyS	Cr, Ce, U, Mn, and Ni form stable sulphates and are not suitable catalysts for sulfuric acid decomposition. t/$BaSO_4$-TiO_2, Pt/TiO_2, Pt/ZrO_2, and Pt/SiO_2 are the most suitable catalysts for the HyS cycle.	[135]
HyS	Pt_xPd_y thin film deposited on a Si wafer showed high catalytic activity	[146]
HyS	Increasing Ni dopant in PtxNiy/C catalysts increased electron vacancies and improved catalytic performance	[148]
HyS	Incorporating ceria in Pt/C composite catalyst increased catalyst active area and improved its performance	[150]
Cu-Cl	Developing a novel integrated system for producing nitrogen, methane, ammonia, oxygen, and carbon dioxide	[168]
Cu-Cl	Optimizing the temperature of the hydrolysis step can minimize the number of byproducts.	[172]
Cu-Cl	Cu-Cl is the most promising cycle for large-scale hydrogen production.	[176]
ZnO/Zn	Partially reduced ZnO showed higher catalytic performance at elevated temperatures (R = 57.2%)	[193]
ZnO/Zn	Hindered recombination and lowered the reaction temperature of the first step (methane or carbon as reducing agent)	[197]
ZnO/Zn	A negative axial temperature gradient reduced the steam and inert gas proportion	[199,202]
SnO_2/SnO	Reducing O_2 partial pressure to about 10^{-3} bar decreased thermal reduction temperature	[209]
Fe_3O_4/FeO	Non-stoichiometric wustite have higher defect densities and showed higher reaction rates	[188]
Ferrite	Zirconia support enhances the energy radiation absorption and lowers the temperature	[186]
Ferrite	Ceramics nanoparticles can slightly increase hydrogen yield and hinder grain growth	[219]
Ferrite	ZrO_2 can reduce the high-temperature sintering and improve catalytic activity	[218]
Ferrite	Calcium-stabilized zirconia forms calcium zirconate promotes high active phase dispersion and improves hydrogen yield	[222]
Ferrite	Sacrificial (carbon black and PEG) and zirconia plates improved the thermal stability of Ni-ferrite samples	[218]
Ferrite	Core-shell $NiFe_2O_4/Y_2O_3$ nanoparticles showed stable hydrogen volume, but lower rates of hydrogen production than that of mixed powders	[219]
Ferrite	Hercynite formation in alumina and cobalt ferrite decreased ferrite reduction temperature	[224]

5. Conclusions

Several efficient thermochemical water-splitting cycles have been discussed above. Each cycle has some strengths and weaknesses. Low-temperature cycles can produce hydrogen at temperatures below 1100 °C. S-I cycle has advantages such as low operating temperature, low costs of materials, continuous flow process, and simple thermal storage concept. However, corrosive compounds, difficulties with non-ideal solutions for predicting equilibrium states with high accuracy, and HI decomposition issues are the main challenges with this cycle. HyS cycle exhibits similar advantages and disadvantages to the S-I cycle but offers lower hydrogen production costs with slightly higher efficiencies. The Cu-Cl cycle requires low voltages, offers desirable hydrogen production costs and high efficiency, and can be further improved using efficient catalysts. To improve the efficiency and long-term durability of the Cu-Cl cycle, some issues such as copper crossover, materials destruction, formation of by-products such as chlorine, and separation of spent anolyte should be addressed.

Among the high-temperature metal oxide cycles, zinc oxide, ferrite, iron oxide, and manganese oxide-based cycles have been discussed. Higher hydrogen yield and lower hydrogen production costs of these cycles are the most important advantages over the other metal oxide cycles. However, some cycles such as BaO/Ba still need further investigations to improve cost-effectiveness. Mixed metal oxides can also be considered potential thermochemical cycles with reduced costs and improved performance. Still, kinetics, long-term stability, economic analysis for large-scale plants, etc., should be addressed and satisfy the required techno-economic targets.

Overall, according to the advantages mentioned earlier and the disadvantages of different cycles, the Cu-Cl cycle seems the most suitable cycle for large-scale hydrogen production. Other cycles such as HyS and nickel ferrite cycles have also shown great potential, but further improvements in efficiency and hydrogen production costs are needed for large-scale applications of these cycles.

Besides the cycle type, the structural and microstructural properties of the materials used in the process should also be optimized to improve the overall efficiency of the cycle. Addressing the material-related challenges and reasonable hydrogen production costs are the two crucial factors for sustainable and cost-effective hydrogen production. Thus, future research should focus on improving the lifetime and efficiency of hydrogen production technologies and operational, maintenance, and capital equipment costs.

Author Contributions: Writing—initial draft preparation, M.F.V.; review, editing B.S.; conceptualization, writing—review, editing, supervision, B.A.H. All authors have read and agreed to the published version of the manuscript.

Funding: Royal Academy of Engineering: LTRF2021\17131.

Institutional Review Board Statement: Not applicable.

Informed Consent Statement: Not applicable.

Conflicts of Interest: The authors declare no conflict of interest.

References

1. Fallah Vostakola, M.; Mirkazemi, S.M.; Eftekhari Yekta, B. Structural, morphological, and optical properties of W-doped VO_2 thin films prepared by sol-gel spin coating method. *Int. J. Appl. Ceram. Technol.* **2019**, *16*, 943–950. [CrossRef]
2. Nguyen, V.H.; Do, H.H.; Van Nguyen, T.; Singh, P.; Raizada, P.; Sharma, A.; Sana, S.S.; Grace, A.N.; Shokouhimehr, M.; Ahn, S.H.; et al. Perovskite oxide-based photocatalysts for solar-driven hydrogen production: Progress and perspectives. *Sol. Energy* **2020**, *211*, 584–599. [CrossRef]
3. Fallah Vostakola, M.; Amini Horri, B. Progress in Material Development for Low-Temperature Solid Oxide Fuel Cells: A Review. *Energies* **2021**, *14*, 1280. [CrossRef]
4. Dincer, I.; Zamfirescu, C. Potential options to greenize energy systems. *Energy* **2012**, *46*, 5–15. [CrossRef]
5. Choolaei, M.; Bull, T.; Ramirez Reina, T.; Amini Horri, B. Synthesis and characterisation of nanocrystalline CuO–Fe2O3/GDC anode powders for solid oxide fuel cells. *Ceram. Int.* **2020**, *46*, 14776–14786. [CrossRef]

6. Clemente, A.; Costa-Castelló, R. Redox flow batteries: A literature review oriented to automatic control. *Energies* **2020**, *13*, 4514. [CrossRef]
7. Schoden, F.; Dotter, M.; Knefelkamp, D.; Blachowicz, T.; Hellkamp, E.S. Review of State of the Art Recycling Methods in the Context of Dye Sensitized Solar Cells. *Energies* **2021**, *14*, 3741. [CrossRef]
8. Rajpar, A.H.; Ali, I.; Eladwi, A.E.; Bashir, M.B.A. Recent Development in the Design of Wind Deflectors for Vertical Axis Wind Turbine: A Review. *Energies* **2021**, *14*, 5140. [CrossRef]
9. Moska, R.; Labus, K.; Kasza, P. Hydraulic Fracturing in Enhanced Geothermal Systems—Field, Tectonic and Rock Mechanics Conditions—A Review. *Energies* **2021**, *14*, 5725. [CrossRef]
10. Le Saché, E.; Johnson, S.; Pastor-Pérez, L.; Horri, B.A.; Reina, T.R. Biogas upgrading via dry reforming over a Ni-Sn/CeO_2-Al_2O_3 catalyst: Influence of the biogas source. *Energies* **2019**, *12*, 1007. [CrossRef]
11. Price, C.A.H.; Arnold, W.; Pastor-Pérez, L.; Amini-Horri, B.; Reina, T.R. Catalytic Upgrading of a Biogas Model Mixture via Low Temperature DRM Using Multicomponent Catalysts. *Top. Catal.* **2020**, *63*, 281–293. [CrossRef]
12. Rezaei, S.E.; Zebarjadi, M.; Esfarjani, K. Effect of exchange-correlation functional type and spin-orbit coupling on thermoelectric properties of $ZrTe_2$. *J. Solid State Chem.* **2021**, *302*, 122414. [CrossRef]
13. Amini Horri, B.; Choolaei, M.; Chaudhry, A.; Qaalib, H. A highly efficient hydrogen generation electrolysis system using alkaline zinc hydroxide solution. *Int. J. Hydrogen Energy* **2019**, *44*, 72–81. [CrossRef]
14. Rafique, M.; Mubashar, R.; Irshad, M.; Gillani, S.S.A.; Tahir, M.B.; Khalid, N.R.; Yasmin, A.; Shehzad, M.A. A Comprehensive Study on Methods and Materials for Photocatalytic Water Splitting and Hydrogen Production as a Renewable Energy Resource. *J. Inorg. Organomet. Polym. Mater.* **2020**, *30*, 3837–3861. [CrossRef]
15. Hooshyari, K.; Amini Horri, B.; Abdoli, H.; Fallah Vostakola, M.; Kakavand, P.; Salarizadeh, P. A Review of Recent Developments and Advanced Applications of High-Temperature Polymer Electrolyte Membranes for PEM Fuel Cells. *Energies* **2021**, *14*, 5440. [CrossRef]
16. Acar, C.; Dincer, I.; Naterer, G.F. Review of photocatalytic water-splitting methods for sustainable hydrogen production. *Int. J. Energy Res.* **2016**, *40*, 1449–1473. [CrossRef]
17. Dincer, I.; Acar, C. Review and evaluation of hydrogen production methods for better sustainability. *Int. J. Hydrogen Energy* **2015**, *40*, 11094–11111. [CrossRef]
18. Brau, J.-F.; Morandin, M.; Berntsson, T. Hydrogen for oil refining via biomass indirect steam gasification: Energy and environmental targets. *Clean Technol. Environ. Policy* **2013**, *15*, 501–512. [CrossRef]
19. Brau, J.F.; Morandin, M. Biomass-based hydrogen for oil refining: Integration and performances of two gasification concepts. *Int. J. Hydrogen Energy* **2014**, *39*, 2531–2542. [CrossRef]
20. Liu, W.; Zuo, H.; Wang, J.; Xue, Q.; Ren, B.; Yang, F. The production and application of hydrogen in steel industry. *Int. J. Hydrogen Energy* **2021**, *46*, 10548–10569. [CrossRef]
21. Dodds, P.E.; Staffell, I.; Hawkes, A.D.; Li, F.; Grünewald, P.; McDowall, W.; Ekins, P. Hydrogen and fuel cell technologies for heating: A review. *Int. J. Hydrogen Energy* **2015**, *40*, 2065–2083. [CrossRef]
22. Felseghi, R.A.; Carcadea, E.; Raboaca, M.S.; Trufin, C.N.; Filote, C. Hydrogen fuel cell technology for the sustainable future of stationary applications. *Energies* **2019**, *12*, 4593. [CrossRef]
23. Bellosta von Colbe, J.; Ares, J.R.; Barale, J.; Baricco, M.; Buckley, C.; Capurso, G.; Gallandat, N.; Grant, D.M.; Guzik, M.N.; Jacob, I.; et al. Application of hydrides in hydrogen storage and compression: Achievements, outlook and perspectives. *Int. J. Hydrogen Energy* **2019**, *44*, 7780–7808. [CrossRef]
24. Cernat, A.; Pana, C.; Negurescu, N.; Lazaroiu, G.; Nutu, C.; Fuiorescu, D. Hydrogen—An alternative fuel for automotive diesel engines used in transportation. *Sustainability* **2020**, *12*, 9321. [CrossRef]
25. Renau, J.; García, V.; Domenech, L.; Verdejo, P.; Real, A.; Giménez, A.; Sánchez, F.; Lozano, A.; Barreras, F. Novel use of green hydrogen fuel cell-based combined heat and power systems to reduce primary energy intake and greenhouse emissions in the building sector. *Sustainability* **2021**, *13*, 1776. [CrossRef]
26. Parra, D.; Valverde, L.; Pino, F.J.; Patel, M.K. A review on the role, cost and value of hydrogen energy systems for deep decarbonisation. *Renew. Sustain. Energy Rev.* **2019**, *101*, 279–294. [CrossRef]
27. Muradov, N.Z.; Veziroğlu, T.N. From hydrocarbon to hydrogen-carbon to hydrogen economy. *Int. J. Hydrogen Energy* **2005**, *30*, 225–237. [CrossRef]
28. Tang, J.; Liu, T.; Miao, S.; Cho, Y. Emerging energy harvesting technology for electro/photo-catalytic water splitting application. *Catalysts* **2021**, *11*, 142. [CrossRef]
29. Yilanci, A.; Dincer, I.; Ozturk, H.K. A review on solar-hydrogen/fuel cell hybrid energy systems for stationary applications. *Prog. Energy Combust. Sci.* **2009**, *35*, 231–244. [CrossRef]
30. Quarton, C.J.; Tlili, O.; Welder, L.; Mansilla, C.; Blanco, H.; Heinrichs, H.; Leaver, J.; Samsatli, N.J.; Lucchese, P.; Robinius, M.; et al. The curious case of the conflicting roles of hydrogen in global energy scenarios. *Sustain. Energy Fuels* **2019**, *4*, 80–95. [CrossRef]
31. Minh, D.P.; Siang, T.J.; Vo, D.V.N.; Phan, T.S.; Ridart, C.; Nzihou, A.; Grouset, D. Hydrogen production from biogas reforming: An overview of steam reforming, dry reforming, dual reforming, and tri-reforming of methane. In *Hydrogen Supply Chain: Design, Deployment and Operation*; Azzaro-Pantel, C., Ed.; Academic Press: Cambridge, MA, USA, 2018; pp. 111–166. ISBN 9780128111970.
32. Howarth, R.W.; Jacobson, M.Z. How green is blue hydrogen? *Energy Sci. Eng.* **2021**, *9*, 1676–1687. [CrossRef]

33. Evers, A.A. A Proposal To Future Energy Supplies: Your Personal Power Provider ($3P^+$) Virtual Power Plants with Direct Solar Hydrogen and Fuel Cells. *I ECS Trans.* **2009**, *17*, 691–696. [CrossRef]
34. Luo, M.; Yi, Y.; Wang, S.; Wang, Z.; Du, M.; Pan, J.; Wang, Q. Review of hydrogen production using chemical-looping technology. *Renew. Sustain. Energy Rev.* **2018**, *81*, 3186–3214. [CrossRef]
35. Wang, Z.; Fan, W.; Zhang, G.; Dong, S. Exergy analysis of methane cracking thermally coupled with chemical looping combustion for hydrogen production. *Appl. Energy* **2016**, *168*, 1–12. [CrossRef]
36. Yang, W.; Moon, J. Recent Advances in Earth-Abundant Photocathodes for Photoelectrochemical Water Splitting. *ChemSusChem* **2019**, *12*, 1889–1899. [CrossRef] [PubMed]
37. Wang, T. An overview of IGCC systems. In *Integrated Gasification Combined Cycle (IGCC) Technologies*; Wang, T., Stiegel, G., Eds.; Elsevier Ltd.: New Orleans, LA, USA, 2017; pp. 1–80. ISBN 9780081001851.
38. Full, J.; Merseburg, S.; Miehe, R.; Sauer, A. A new perspective for climate change mitigation— introducing carbon-negative hydrogen production from biomass with carbon capture and storage (Hybeccs). *Sustainability* **2021**, *13*, 4026. [CrossRef]
39. Vedyagin, A.A.; Mishakov, I.V.; Korneev, D.V.; Bauman, Y.I.; Nalivaiko, A.Y.; Gromov, A.A. Selected Aspects of Hydrogen Production via Catalytic Decomposition of Hydrocarbons. *Hydrogen* **2021**, *2*, 122–133. [CrossRef]
40. Speight, J.G. Synthesis gas and the Fischer–Tropsch process. In *The Refinery of the Future*; Speight, J.G., Ed.; Gulf Professional Publishing: Laramie, WY, USA, 2020; pp. 427–468. ISBN 9780128169940.
41. Lamb, J.J.; Hillestad, M.; Rytter, E.; Bock, R.; Nordgård, A.S.R.; Lien, K.M.; Burheim, O.S.; Pollet, B.G. Traditional Routes for Hydrogen Production and Carbon Conversion. In *Hydrogen, Biomass and Bioenergy*; Lamb, J.J., Pollet, B.G., Eds.; Elsevier Ltd.: Trondheim, Norway, 2020; pp. 21–53. ISBN 9780081026298.
42. Chen, G.; Tao, J.; Liu, C.; Yan, B.; Li, W.; Li, X. Hydrogen production via acetic acid steam reforming: A critical review on catalysts. *Renew. Sustain. Energy Rev.* **2017**, *79*, 1091–1098. [CrossRef]
43. Go, K.S.; Son, S.R.; Kim, S.D.; Kang, K.S.; Park, C.S. Hydrogen production from two-step steam methane reforming in a fluidized bed reactor. *Int. J. Hydrogen Energy* **2009**, *34*, 1301–1309. [CrossRef]
44. Li, L.; Jiang, B.; Sun, Z.; Zhang, Q.; Li, D.; Tang, D. Hydrogen production from chemical looping steam reforming of ethanol over perovskite-type oxygen carriers with bimetallic Co and Ni B-site substitution. *Catalysts* **2018**, *8*, 372. [CrossRef]
45. Alobaid, F.; Ströhle, J. Special issue "thermochemical conversion processes for solid fuels and renewable energies". *Appl. Sci.* **2021**, *11*, 1907. [CrossRef]
46. Dou, B.; Zhang, H.; Cui, G.; Wang, Z.; Jiang, B.; Wang, K.; Chen, H.; Xu, Y. Hydrogen production by sorption-enhanced chemical looping steam reforming of ethanol in an alternating fixed-bed reactor: Sorbent to catalyst ratio dependencies. *Energy Convers. Manag.* **2018**, *155*, 243–252. [CrossRef]
47. Pujara, M.; Sheth, M.; Rachchh, N.; Bhoraniya, R.; Harichandan, A.B. Chemical Looping Reforming (CLR) System for H2 Production—A Review. In *Renewable Energy and Climate Change-Proceedings of REC 2019*; Deb, D., Dixit, A., Chandra, L., Eds.; Springer: Berlin/Heidelberg, Germany, 2020; Volume 161, pp. 267–276. ISBN 9789813295773.
48. Tang, M.; Xu, L.; Fan, M. Progress in oxygen carrier development of methane-based chemical-looping reforming: A review. *Appl. Energy* **2015**, *151*, 143–156. [CrossRef]
49. Wang, K.; Dou, B.; Jiang, B.; Song, Y.; Zhang, C.; Zhang, Q.; Chen, H.; Xu, Y. Renewable hydrogen production from chemical looping steam reforming of ethanol using xCeNi/SBA-15 oxygen carriers in a fixed-bed reactor. *Int. J. Hydrogen Energy* **2016**, *41*, 12899–12909. [CrossRef]
50. Muriungi, B.; Wang, L.; Shahbazi, A. Comparison of bimetallic Fe-Cu and Fe-Ca oxygen carriers for biomass gasification. *Energies* **2020**, *13*, 2019. [CrossRef]
51. O'Malley, K.; Donat, F.; Whitty, K.J.; Sohn, H.Y. Scalable Preparation of Bimetallic Cu/Ni-Based Oxygen Carriers for Chemical Looping. *Energy Fuels* **2020**, *34*, 11227–11236. [CrossRef]
52. Wei, G.; He, F.; Zhao, Z.; Huang, Z.; Zheng, A.; Zhao, K.; Li, H. Performance of Fe-Ni bimetallic oxygen carriers for chemical looping gasification of biomass in a 10 kWth interconnected circulating fluidized bed reactor. *Int. J. Hydrogen Energy* **2015**, *40*, 16021–16032. [CrossRef]
53. Hossain, M.M.; Lasa, H.I. de Reactivity and Stability of Co-Ni/Al_2O_3 Oxygen Carrier in Multicycle CLC. *React. Kinet. Catal.* **2007**, *53*, 1817–1829. [CrossRef]
54. Li, L.; Song, Y.; Jiang, B.; Wang, K.; Zhang, Q. A novel oxygen carrier for chemical looping reforming: $LaNiO_3$ perovskite supported on montmorillonite. *Energy* **2017**, *131*, 58–66. [CrossRef]
55. Liu, L.; Li, Z.; Li, Z.; Larring, Y.; Cai, N. Perovskite oxygen carrier with chemical memory under reversible chemical looping conditions with and without SO2 during reduction. *Chem. Eng. J.* **2021**, *424*, 130417. [CrossRef]
56. Hamrang, F.; Seyed Mahmoudi, S.M.; Rosen, M.A. A novel electricity and freshwater production system: Performance analysis from reliability and exergoeconomic viewpoints with multi-objective optimization. *Sustainability* **2021**, *13*, 6448. [CrossRef]
57. Miller, B.G. Clean Coal Technologies for Advanced Power Generation. In *Clean Coal Engineering Technology*; Elsevier Inc.: Amsterdam, The Netherlands, 2017; pp. 261–308. ISBN 9780128113653.
58. Huang, D.; Zhang, H.; Weng, S.; Su, M. Modeling and simulation of IGCC considering pressure and flow distribution of gasifier. *Appl. Sci.* **2016**, *6*, 292. [CrossRef]

59. Cormos, C.C.; Cormos, A.M.; Serban Agachi, P. Techno-economical and environmental evaluations of IGCC power generation process with carbon capture and storage (CCS). In *Computer Aided Chemical Engineering Computer*; Pistikopoulos, E.N., Georgiadis, M.C., Kokossis, A.C., Eds.; Elsevier: Amsterdam, The Netherlands, 2011; Volume 29, pp. 1678–1682.
60. Hwang, B.; Kim, J.H.; Lee, D.; Nam, H.; Kim, H.N.; Baek, J.I.; Ryu, H.J. Investigation on the cause of the so2 generation during hot gas desulfurization (Hgd) process. *Catalysts* **2021**, *11*, 985. [CrossRef]
61. Kaldis, S.P.; Pantoleontos, G.T.; Koutsonikolas, D.E. Membrane technology in IGCC processes for precombustion CO_2 capture. In *Current Trends and Future Developments on (Bio-) Membranes: Carbon Dioxide Separation/Capture by Using Membranes*; Basile, A., Favvas, E.P., Eds.; Elsevier: Thessaloniki, Greece, 2018; pp. 329–357. ISBN 9780128136454.
62. Tzimas, E.; Mercier, A.; Cormos, C.C.; Peteves, S.D. Trade-off in emissions of acid gas pollutants and of carbon dioxide in fossil fuel power plants with carbon capture. *Energy Policy* **2007**, *35*, 3991–3998. [CrossRef]
63. Hossein Sahraei, M.; McCalden, D.; Hughes, R.; Ricardez-Sandoval, L.A. A survey on current advanced IGCC power plant technologies, sensors and control systems. *Fuel* **2014**, *137*, 245–259. [CrossRef]
64. Gholamian, E.; Mahmoudi, S.M.S.; Zare, V. Proposal, exergy analysis and optimization of a new biomass-based cogeneration system. *Appl. Therm. Eng.* **2016**, *93*, 223–235. [CrossRef]
65. Safarian, S.; Ebrahimi Saryazdi, S.M.; Unnthorsson, R.; Richter, C. Modeling of hydrogen production by applying biomass gasification: Artificial neural network modeling approach. *Fermentation* **2021**, *7*, 71. [CrossRef]
66. Zhang, X.; Zhou, Y.; Jia, X.; Feng, Y.; Dang, Q. Multi-Criteria Optimization of a Biomass-Based Hydrogen Production System Integrated With Organic Rankine Cycle. *Front. Energy Res.* **2020**, *8*, 584215. [CrossRef]
67. Kaskun, S. An overview of hydrogen-rich gas production from biomass by using thermal technologies. *IOP Conf. Ser. Earth Environ. Sci.* **2020**, *614*, 012010. [CrossRef]
68. Safarian, S.; Unnþórsson, R.; Richter, C. A review of biomass gasification modelling. *Renew. Sustain. Energy Rev.* **2019**, *110*, 378–391. [CrossRef]
69. Meramo-Hurtado, S.I.; Puello, P.; Cabarcas, A. Process analysis of hydrogen production via biomass gasification under computer-aided safety and environmental assessments. *ACS Omega* **2020**, *5*, 19667–19681. [CrossRef]
70. Safarian, S.; Unnthorsson, R.; Richter, C. Performance analysis and environmental assessment of small-scale waste biomass gasification integrated CHP in Iceland. *Energy* **2020**, *197*, 117268. [CrossRef]
71. Ji, P.; Feng, W.; Chen, B. Comprehensive simulation of an intensified process for H2 production from steam gasification of biomass. *Ind. Eng. Chem. Res.* **2009**, *48*, 3909–3920. [CrossRef]
72. Wu, H.; Liu, Q.; Bai, Z.; Xie, G.; Zheng, J.; Su, B. Thermodynamics analysis of a novel steam/air biomass gasification combined cooling, heating and power system with solar energy. *Appl. Therm. Eng.* **2020**, *164*, 114494. [CrossRef]
73. Zhang, S.; Gao, N.; Quan, C.; Wang, F.; Wu, C. Autothermal CaO looping biomass gasification to increase process energy efficiency and reduce ash sintering. *Fuel* **2020**, *277*, 118199. [CrossRef]
74. Ishaq, H.; Islam, S.; Dincer, I.; Yilbas, B.S. Development and performance investigation of a biomass gasification based integrated system with thermoelectric generators. *J. Clean. Prod.* **2020**, *256*, 120625. [CrossRef]
75. Ebrahimi, A.; Ziabasharhagh, M. Energy and exergy analyses of a novel integrated process configuration for tri-generation heat, power and liquefied natural gas based on biomass gasification. *Energy Convers. Manag.* **2020**, *209*, 112624. [CrossRef]
76. Megía, P.J.; Calles, J.A.; Carrero, A.; Vizcaíno, A.J. Effect of the incorporation of reducibility promoters (Cu, Ce, Ag) in Co/CaSBA-15 catalysts for acetic acid steam reforming. *Int. J. Energy Res.* **2021**, *45*, 1685–1702. [CrossRef]
77. Zhang, L.; Yu, Z.; Li, J.; Zhang, S.; Hu, S.; Xiang, J.; Wang, Y.; Liu, Q.; Hu, G.; Hu, X. Steam reforming of typical small organics derived from bio-oil: Correlation of their reaction behaviors with molecular structures. *Fuel* **2020**, *259*, 116214. [CrossRef]
78. Martino, M.; Ruocco, C.; Meloni, E.; Pullumbi, P.; Palma, V. Main hydrogen production processes: An overview. *Catalysts* **2021**, *11*, 547. [CrossRef]
79. Palma, V.; Ruocco, C.; Cortese, M.; Martino, M. Bioalcohol reforming: An overview of the recent advances for the enhancement of catalyst stability. *Catalysts* **2020**, *10*, 665. [CrossRef]
80. Hou, X.; Qing, S.; Liu, Y.; Li, L.; Gao, Z.; Qin, Y. Enhancing effect of MgO modification of Cu–Al spinel oxide catalyst for methanol steam reforming. *Int. J. Hydrogen Energy* **2020**, *45*, 477–489. [CrossRef]
81. López-Martín, A.; Platero, F.; Caballero, A.; Colón, G. Thermo-Photocatalytic Methanol Reforming for Hydrogen Production over a CuPd−TiO_2 Catalyst. *ChemPhotoChem* **2020**, *4*, 630–637. [CrossRef]
82. Yu, C.L.; Sakthinathan, S.; Hwang, B.Y.; Lin, S.Y.; Chiu, T.W.; Yu, B.S.; Fan, Y.J.; Chuang, C. $CuFeO_2$–CeO_2 nanopowder catalyst prepared by self-combustion glycine nitrate process and applied for hydrogen production from methanol steam reforming. *Int. J. Hydrogen Energy* **2020**, *45*, 15752–15762. [CrossRef]
83. Mateos-Pedrero, C.; Azenha, C.; Pacheco, P.T.; Sousa, J.M.; Mendes, A. The influence of the support composition on the physicochemical and catalytic properties of Cu catalysts supported on Zirconia-Alumina for methanol steam reforming. *Appl. Catal. B Environ.* **2020**, *277*, 119243. [CrossRef]
84. Shelepova, E.V.; Vedyagin, A.A. Theoretical Prediction of the Efficiency of Hydrogen Production via Alkane Dehydrogenation in Catalytic Membrane Reactor. *Hydrogen* **2021**, *2*, 362–376. [CrossRef]
85. Shelepova, E.V.; Vedyagin, A.A.; Mishakov, I.V.; Noskov, A.S. Mathematical modeling of the propane dehydrogenation process in the catalytic membrane reactor. *Chem. Eng. J.* **2011**, *176–177*, 151–157. [CrossRef]

86. Shelepova, E.V.; Vedyagin, A.A.; Mishakov, I.V.; Noskov, A.S. Simulation of hydrogen and propylene coproduction in catalytic membrane reactor. *Int. J. Hydrogen Energy* **2015**, *40*, 3592–3598. [CrossRef]
87. Li, Y.; Zhang, Z.; Jia, P.; Dong, D.; Wang, Y.; Hu, S.; Xiang, J.; Liu, Q.; Hu, X. Ethanol steam reforming over cobalt catalysts: Effect of a range of additives on the catalytic behaviors. *J. Energy Inst.* **2020**, *93*, 165–184. [CrossRef]
88. Greluk, M.; Rotko, M.; Turczyniak-Surdacka, S. Enhanced catalytic performance of La_2O_3 promoted Co/CeO_2 and Ni/CeO_2 catalysts for effective hydrogen production by ethanol steam reforming: La_2O_3 promoted $Co(Ni)/CeO_2$ catalysts in SRE. *Renew. Energy* **2020**, *155*, 378–395. [CrossRef]
89. Martinelli, M.; Watson, C.D.; Jacobs, G. Sodium doping of $Pt/m\text{-}ZrO_2$ promotes C–C scission and decarboxylation during ethanol steam reforming. *Int. J. Hydrogen Energy* **2020**, *45*, 18490–18501. [CrossRef]
90. Tyagi, D.; Shirsat, A.N.; Varma, S. Carbon derived from rice: Application as a support for platinum catalysts for hydrogen generation by HI decomposition. *Bull. Mater. Sci.* **2021**, *44*, 172. [CrossRef]
91. Juárez-Martínez, L.C.; Espinosa-Paredes, G.; Vázquez-Rodríguez, A.; Romero-Paredes, H. Energy optimization of a Sulfur–Iodine thermochemical nuclear hydrogen production cycle. *Nucl. Eng. Technol.* **2021**, *53*, 2066–2073. [CrossRef]
92. Lassouane, F.; Menia, S.; Khellaf, A. An overview of the hybrid sulfur cycle process for solar hydrogen production. In *Proceedings of the 3rd International Symposium on Environment Friendly Energies and Applications, EFEA 2014*; IEEE: Paris, France, 2014; pp. 1–6.
93. Vagia, E.C.; Muradov, N.; Kalyva, A.; T-Raissi, A.; Qin, N.; Srinivasa, A.R.; Kakosimos, K.E. Solar hybrid photo-thermochemical sulfur-ammonia water-splitting cycle: Photocatalytic hydrogen production stage. *Int. J. Hydrogen Energy* **2017**, *42*, 20608–20624. [CrossRef]
94. Dincer, I.; Zamfirescu, C. Other Hydrogen Production Methods. In *Sustainable Hydrogen Production*; Elsevier Inc.: Amsterdam, The Netherlands, 2016; pp. 411–439. ISBN 9780128015636.
95. Acar, C.; Dincer, I. Hydrogen Production. In *Comprehensive Energy Systems*; Elsevier: Amsterdam, The Netherlands, 2018; Volume 3, pp. 1–40. ISBN 9780128095973.
96. Abanades, S. Metal Oxides Applied to Thermochemical Water-Splitting for Hydrogen Production Using Concentrated Solar Energy. *ChemEngineering* **2019**, *3*, 63. [CrossRef]
97. Steinfeld, A. Solar thermochemical production of hydrogen—A review. *Sol. Energy* **2005**, *78*, 603–615. [CrossRef]
98. Perkins, C.; Weimer, A.W. Solar-Thermal Production of Renewable Hydrogen. *AIChE J.* **2009**, *55*, 286–293. [CrossRef]
99. O'keefe, D.R.; Allen, C.L.; Besenbruch, G.; Brown, L.; Norman, J.H.; Sharp, R.; Mccorkle, K.H. Preliminary results from bench-scale testing of a sulfur-iodine thermochemical water-splitting cycle. *Int. J. Hydrogen Energy* **1982**, *7*, 381–392. [CrossRef]
100. Park, J.; Lee, S.Y.; Lee, I.B. Study of alternative reactor-separator network in bunsen process of sulfur-iodine cycle for hydrogen production. *J. Chem. Eng. Jpn.* **2019**, *52*, 638–649. [CrossRef]
101. Boretti, A.; Nayfeh, J.; Al-Maaitah, A. Hydrogen Production by Solar Thermochemical Water-Splitting Cycle via a Beam Down Concentrator. *Front. Energy Res.* **2021**, *9*, 666191. [CrossRef]
102. Li, X.; Zhang, R.; Zhu, X.; Zhang, L. Effect of N-doping on the catalytic decomposition of hydrogen iodide over activated carbon: Experimental and DFT studies. *Int. J. Hydrogen Energy* **2020**, *45*, 4511–4520. [CrossRef]
103. Grimes, C.A.; Varghese, O.; Ranjan, S. Hydrogen Generation by Water Splitting. In *Light, Water, Hydrogen*; Springer: New York, NY, USA, 2008; pp. 35–113. ISBN 9780126552812.
104. Giaconia, A.; Caputo, G.; Ceroli, A.; Diamanti, M.; Barbarossa, V.; Tarquini, P.; Sau, S. Experimental study of two phase separation in the Bunsen section of the sulfur-iodine thermochemical cycle. *Int. J. Hydrogen Energy* **2007**, *32*, 531–536. [CrossRef]
105. Dincer, I.; Bicer, Y. Solar Thermochemical Energy Conversion. In *Comprehensive Energy Systems*; Dincer, I., Ed.; Elsevier: Amsterdam, The Netherlands, 2018; Volume 4b, pp. 895–946. ISBN 9780128095973.
106. Perret, R. *Solar Thermochemical Hydrogen Production Research (STCH) Thermochemical Cycle Selection and Investment Priority*; Document number: SAND2011-3622; Sandia National Laboratories: Albuquerque, NM, USA, 2011; pp. 1–117.
107. Zhu, Q.; Zhang, Y.; Zhou, C.; Wang, Z.; Zhou, J.; Cen, K. Optimization of liquid-liquid phase separation characteristics in the Bunsen section of the sulfur-iodine hydrogen production process. *Int. J. Hydrogen Energy* **2012**, *37*, 6407–6414. [CrossRef]
108. Roeb, M.; Neises, M.; Monnerie, N.; Call, F.; Simon, H.; Sattler, C.; Schmücker, M.; Pitz-Paal, R. Materials-related aspects of thermochemical water and carbon dioxide splitting: A review. *Materials* **2012**, *5*, 2015–2054. [CrossRef]
109. Hong, D.; Kim, H.; Kim, Y.; Park, C.; Bae, K. The Role of Oxygen in Bunsen Reaction Section of Sulfur-Iodine Hydrogen Production Process. *Trans. Korean Hydrog. New Energy Soc.* **2010**, *21*, 278–285.
110. Ying, Z.; Yang, J.; Zheng, X.; Wang, Y.; Dou, B. Energy and exergy analyses of a novel sulfur–iodine cycle assembled with $HI–I_2–H_2O$ electrolysis for hydrogen production. *Int. J. Hydrogen Energy* **2021**, *46*, 23139–23148. [CrossRef]
111. Singhania, A.; Bhaskarwar, A.N. Development of catalysts for hydrogen production from hydrogen iodide decomposition in thermo-chemical water-splitting sulfur-iodine cycle: A review. *Catal. Rev.-Sci. Eng.* **2017**, *59*, 446–489. [CrossRef]
112. Ying, Z.; Zhang, Y.; Zheng, X.; Cui, G. Performance of electrochemical cell with various flow channels for Bunsen reaction in the sulfur–iodine hydrogen production process. *Energy Convers. Manag.* **2017**, *151*, 514–523. [CrossRef]
113. Zhang, K.; Zhao, X.; Chen, S.; Chang, L.; Wang, J.; Bao, W.; Wang, H. Direct electrolysis of Bunsen reaction product $HI/H_2SO_4/H_2O$/toluene mixture for hydrogen production: Pt electrode characterization. *Int. J. Hydrogen Energy* **2018**, *43*, 13702–13710. [CrossRef]
114. Zhang, K.; Bao, W.; Chang, L.; Wang, H. A review of recent researches on Bunsen reaction for hydrogen production via S–I water and H_2S splitting cycles. *J. Energy Chem.* **2019**, *33*, 46–58. [CrossRef]

115. Yu, X.; Meng, L.; Nagasawa, H.; Kanezashi, M.; Machida, M.; Tsuru, T. Evaluating the chemical stability of metal oxides in SO_3 and applications of SiO_2-based membranes to O_2/SO_3 separation. *J. Am. Ceram. Soc.* **2019**, *102*, 6946–6956. [CrossRef]
116. Park, J.K.; Ifaei, P.; Ba-Alawi, A.H.; Safder, U.; Yoo, C.K. Hydrogen production through the sulfur–iodine cycle using a steam boiler heat source for risk and techno-socio-economic cost (RSTEC) reduction. *Int. J. Hydrogen Energy* **2020**, *45*, 14578–14593. [CrossRef]
117. Rong, S.; Zhang, R.; Zhu, X.; Zhang, M.; Li, J.; Zhang, L. Exploring the relationship between the physical properties of activated carbon catalysts and their efficiency in catalyzing hydrogen iodide decomposition to produce hydrogen. *Int. J. Hydrogen Energy* **2021**, *46*, 18207–18223. [CrossRef]
118. Kim, J.M.; Park, J.E.; Kim, Y.H.; Kang, K.S.; Kim, C.H.; Park, C.S.; Bae, K.K. Decomposition of hydrogen iodide on Pt/C-based catalysts for hydrogen production. *Int. J. Hydrogen Energy* **2008**, *33*, 4974–4980. [CrossRef]
119. Wang, Z.C.; Wang, L.J.; Zhang, P.; Chen, S.Z.; Xu, J.M.; Chen, J. Effect of preparation methods on Pt/alumina catalysts for the hydrogen iodide catalytic decomposition. *Chinese Chem. Lett.* **2009**, *20*, 102–105. [CrossRef]
120. Zhang, Y.W.; Wang, Z.; Zhou, J.; Liu, J.; Cen, K. Effect of preparation method on platinum-ceria catalysts for hydrogen iodide decomposition in sulfur-iodine cycle. *Int. J. Hydrogen Energy* **2008**, *33*, 602–607. [CrossRef]
121. Zhang, Y.; Wang, Z.; Zhou, J.; Liu, J.; Cen, K. Experimental study of Ni/CeO_2 catalytic properties and performance for hydrogen production in sulfur-iodine cycle. *Int. J. Hydrogen Energy* **2009**, *34*, 5637–5644. [CrossRef]
122. Singhania, A.; Bhaskarwar, A.N. Catalytic performance of carbon nanotubes supported palladium catalyst for hydrogen production from hydrogen iodide decomposition in thermochemical sulfur iodine cycle. *Renew. Energy* **2018**, *127*, 509–513. [CrossRef]
123. Tyagi, D.; Varma, S.; Bharadwaj, S.R. Pt/zirconia catalyst for hydrogen generation from HI decomposition reaction of S–I cycle. *Int. J. Energy Res.* **2015**, *39*, 484–493. [CrossRef]
124. Tyagi, D.; Varma, S.; Bharadwaj, S.R. Pt/graphite catalyst for hydrogen generation by HI decomposition reaction in S–I thermochemical cycle. *Int. J. Energy Res.* **2015**, *39*, 2008–2018. [CrossRef]
125. Petkovic, L.M.; Ginosar, D.M.; Rollins, H.W.; Burch, K.C.; Deiana, C.; Silva, H.S.; Sardella, M.F.; Granados, D. Activated carbon catalysts for the production of hydrogen via the sulfur-iodine thermochemical water splitting cycle. *Int. J. Hydrogen Energy* **2009**, *34*, 4057–4064. [CrossRef]
126. Wang, Z.; Chen, Y.; Zhou, C.; Whiddon, R.; Zhang, Y.; Zhou, J.; Cen, K. Decomposition of hydrogen iodide via wood-based activated carbon catalysts for hydrogen production. *Int. J. Hydrogen Energy* **2011**, *36*, 216–223. [CrossRef]
127. Lin, X.; Zhang, Y.; Wang, R.; Wang, Z.; Zhou, J.; Cen, K. Influence of the structural and surface characteristics of activated carbon on the catalytic decomposition of hydrogen iodide in the sulfur-iodine cycle for hydrogen production. *Int. J. Hydrogen Energy* **2013**, *38*, 15003–15011. [CrossRef]
128. Everson, R.C.; Stander, B.F.; Neomagus, H.W.J.P.; Van Der Merwe, A.F.; Le Grange, L.; Tietz, M.R. Sulphur trioxide decomposition with supported platinum/palladium on rutile catalysts: 1. Reaction kinetics of catalyst pellets. *Int. J. Hydrogen Energy* **2015**, *40*, 85–94. [CrossRef]
129. Banerjee, A.M.; Pai, M.R.; Tewari, R.; Raje, N.; Tripathi, A.K.; Bharadwaj, S.R.; Das, D. A comprehensive study on Pt/Al_2O_3 granular catalyst used for sulfuric acid decomposition step in sulfur-iodine thermochemical cycle: Changes in catalyst structure, morphology and metal-support interaction. *Appl. Catal. B Environ.* **2015**, *162*, 327–337. [CrossRef]
130. Nur, A.S.M.; Matsukawa, T.; Hinokuma, S.; Machida, M. Catalytic SO_3 decomposition activity and stability of Pt supported on anatase TiO_2 for solar thermochemical water-splitting cycles. *ACS Omega* **2017**, *2*, 7057–7065. [CrossRef]
131. Kawada, T.; Ikematsu, A.; Tajiri, T.; Takeshima, S.; Machida, M. Structure and SO_3 decomposition activity of $CeVO_4/SiO_2$ catalysts for solar thermochemical water splitting cycles. *Int. J. Hydrogen Energy* **2015**, *40*, 10726–10733. [CrossRef]
132. Wang, L.; Zhu, Y.; Yang, H.; He, Y.; Xia, J.; Zhang, Y.; Wang, Z. SO_3 decomposition over $CuO–CeO_2$ based catalysts in the sulfur–iodine cycle for hydrogen production. *Int. J. Hydrogen Energy* **2018**, *43*, 14876–14884. [CrossRef]
133. Jianu, O.A.; Naterer, G.F.; Rosen, M.A. Hydrogen cogeneration with generation IV nuclear power plants. In *Handbook of Generation IV Nuclear Reactors*; Pioro, I.L., Ed.; Elsevier Ltd.: Amsterdam, The Netherlands, 2016; pp. 637–659. ISBN 9780081001622.
134. Roeb, M.; Monnerie, N.; Houaijia, A.; Thomey, D.; Sattler, C. Solar Thermal Water Splitting. In *Renewable Hydrogen Technologies: Production, Purification, Storage, Applications and Safety*; Elsevier: Amsterdam, The Netherlands, 2013; pp. 63–86. ISBN 9780444563521.
135. Corgnale, C.; Gorensek, M.B.; Summers, W.A. Review of sulfuric acid decomposition processes for sulfur-based thermochemical hydrogen production cycles. *Processes* **2020**, *8*, 1383. [CrossRef]
136. Corgnale, C.; Summers, W.A. Solar hydrogen production by the Hybrid Sulfur process. *Int. J. Hydrogen Energy* **2011**, *36*, 11604–11619. [CrossRef]
137. Staser, J.A.; Gorensek, M.B.; Weidner, J.W. Quantifying Individual Potential Contributions of the Hybrid Sulfur Electrolyzer. *J. Electrochem. Soc.* **2010**, *157*, B952. [CrossRef]
138. Steimke, J.L.; Steeper, T.J.; Cólon-Mercado, H.R.; Gorensek, M.B. Development and testing of a PEM SO2-depolarized electrolyzer and an operating method that prevents sulfur accumulation. *Int. J. Hydrogen Energy* **2015**, *40*, 13281–13294. [CrossRef]
139. Garrick, T.R.; Wilkins, C.H.; Pingitore, A.T.; Mehlhoff, J.; Gulledge, A.; Benicewicz, B.C.; Weidner, J.W. Characterizing Voltage Losses in an SO_2 Depolarized Electrolyzer Using Sulfonated Polybenzimidazole Membranes. *J. Electrochem. Soc.* **2017**, *164*, F1591–F1595. [CrossRef]

140. Meekins, B.H.; Thompson, A.B.; Gopal, V.; Mehrabadi, B.A.T.; Elvington, M.C.; Ganesan, P.; Newhouse-Illige, T.A.; Shepard, A.W.; Scipioni, L.E.; Greer, J.A.; et al. In-situ and ex-situ comparison of the electrochemical oxidation of SO_2 on carbon supported Pt and Au catalysts. *Int. J. Hydrogen Energy* **2020**, *45*, 1940–1947. [CrossRef]
141. Brown, N.R.; Revankar, S.T. A review of catalytic sulfur (VI) oxide decomposition experiments. *Int. J. Hydrogen Energy* **2012**, *37*, 2685–2698. [CrossRef]
142. Colón-Mercado, H.R.; Hobbs, D.T. Catalyst evaluation for a sulfur dioxide-depolarized electrolyzer. *Electrochem. commun.* **2007**, *9*, 2649–2653. [CrossRef]
143. Kim, T.H.; Gong, G.T.; Lee, B.G.; Lee, K.Y.; Jeon, H.Y.; Shin, C.H.; Kim, H.; Jung, K.D. Catalytic decomposition of sulfur trioxide on the binary metal oxide catalysts of Fe/Al and Fe/Ti. *Appl. Catal. A Gen.* **2006**, *305*, 39–45. [CrossRef]
144. Díaz-Abad, S.; Millán, M.; Rodrigo, M.A.; Lobato, J. Review of anodic catalysts for SO_2 depolarized electrolysis for "green hydrogen" production. *Catalysts* **2019**, *9*, 63. [CrossRef]
145. Seo, E.T.; Sawyer, D.T. Electrochemical oxidation of dissolved sulphur dioxide at platinum and gold electrodes. *Electrochim. Acta* **1965**, *10*, 239–252. [CrossRef]
146. Falch, A.; Lates, V.; Kriek, R.J. Combinatorial Plasma Sputtering of PtxPdy Thin Film Electrocatalysts for Aqueous SO_2 Electro-oxidation. *Electrocatalysis* **2015**, *6*, 322–330. [CrossRef]
147. Falch, A.; Lates, V.A.; Kotzé, H.S.; Kriek, R.J. The Effect of Rapid Thermal Annealing on Sputtered Pt and Pt_3Pd_2 Thin Film Electrocatalysts for Aqueous SO_2 Electro-Oxidation. *Electrocatalysis* **2016**, *7*, 33–41. [CrossRef]
148. Zhang, S.; Huang, B.; He, Y.; Zhu, Y.; Zhang, Y.; Wang, Z. Demetallized PtxNiy/C catalyst for SO_2 electrochemical oxidation in the SI/HyS hydrogen production cycles. *Int. J. Hydrogen Energy* **2021**, *46*, 10161–10171. [CrossRef]
149. Xue, L.; Zhang, P.; Chen, S.; Wang, L. Pt-based bimetallic catalysts for SO_2-depolarized electrolysis reaction in the hybrid sulfur process. *Int. J. Hydrogen Energy* **2014**, *39*, 14196–14203. [CrossRef]
150. Xu, F.; Cheng, K.; Yu, Y.; Mu, S. One-pot synthesis of $Pt/CeO_2/C$ catalyst for enhancing the SO_2 electrooxidation. *Electrochim. Acta* **2017**, *229*, 253–260. [CrossRef]
151. Jayakumar, J.V.; Gulledge, A.; Staser, J.A.; Kim, C.H.; Benicewicz, B.C.; Weidner, J.W. Polybenzimidazole membranes for hydrogen and sulfuric acid production in the hybrid sulfur electrolyzer. *ECS Electrochem. Lett.* **2012**, *1*, 44–48. [CrossRef]
152. Taylor, R.; Davenport, R.; Talbot, J.; Herz, R.; Luc, W.; Genders, D.; Symons, P.; Brown, L. Status of the solar sulfur ammonia thermochemical hydrogen production system for splitting water. *Energy Procedia* **2014**, *49*, 2047–2058. [CrossRef]
153. Shazed, A.R.; Kalyva, A.E.; Vagia, E.C.; Srinivasa, A.R.; Traissi, A.; Muradov, N.; Kakosimos, K.E. Chemical plant analysis of hydrogen production based on the hybrid sulfur-ammonia water splitting cycle. *Chem. Eng. Trans.* **2017**, *61*, 433–438. [CrossRef]
154. Littlefield, J.; Wang, M.; Brown, L.C.; Herz, R.K.; Talbot, J.B. Process modeling and thermochemical experimental analysis of a solar sulfur ammonia hydrogen production cycle. *Energy Procedia* **2012**, *29*, 616–623. [CrossRef]
155. T-Raissi, A.; Muradov, N.; Huang, C.; Adebiyi, O. Hydrogen from solar via light-assisted high-temperature water splitting cycles. *J. Sol. Energy Eng. Trans. ASME* **2007**, *129*, 184–189. [CrossRef]
156. Gorensek, M.B.; Corgnale, C.; Summers, W.A. Development of the hybrid sulfur cycle for use with concentrated solar heat. I. Conceptual design. *Int. J. Hydrogen Energy* **2017**, *42*, 20939–20954. [CrossRef]
157. Niehoff, A.G.; Botero, N.B.; Acharya, A.; Thomey, D.; Roeb, M.; Sattler, C.; Pitz-Paal, R. Process modelling and heat management of the solar hybrid sulfur cycle. *Int. J. Hydrogen Energy* **2015**, *40*, 4461–4473. [CrossRef]
158. Bilgen, E. Solar hydrogen production by hybrid thermochemical processes. *Sol. Energy* **1988**, *41*, 199–206. [CrossRef]
159. Bhosale, R.R.; Sutar, P.; Kumar, A.; Almomani, F.; Ali, M.H.; Ghosh, U.; Almuhtaseb, S.; Khraisheh, M. Solar hydrogen production via erbium oxide based thermochemical water splitting cycle. *J. Renew. Sustain. Energy* **2016**, *8*, 034702. [CrossRef]
160. Yao, W.; Song, X.; Huang, C.; Xu, Q.; Wu, Q. Enhancing solar hydrogen production via modified photochemical treatment of Pt/CdS photocatalyst. *Catal. Today* **2013**, *199*, 42–47. [CrossRef]
161. Yao, W.; Huang, C.; Muradov, N.; T-Raissi, A. A novel Pd-Cr2O3/CdS photocatalyst for solar hydrogen production using a regenerable sacrificial donor. *Int. J. Hydrogen Energy* **2011**, *36*, 4710–4715. [CrossRef]
162. Chen, X.; Shen, S.; Guo, L.; Mao, S.S. Semiconductor-based photocatalytic hydrogen generation. *Chem. Rev.* **2010**, *110*, 6503–6570. [CrossRef]
163. Zhang, N.; Chen, D.; Cai, B.; Wang, S.; Niu, F.; Qin, L.; Huang, Y. Facile synthesis of CdS-$ZnWO_4$ composite photocatalysts for efficient visible light driven hydrogen evolution. *Int. J. Hydrogen Energy* **2017**, *42*, 1962–1969. [CrossRef]
164. Preethi, V.; Kanmani, S. Photocatalytic hydrogen production using Fe_2O_3-based core shell nano particles with ZnS and CdS. *Int. J. Hydrogen Energy* **2014**, *39*, 1613–1622. [CrossRef]
165. Chen, R.; Li, K.; Zhu, X.S.; Xie, S.L.; Dong, L.Z.; Li, S.L.; Lan, Y.Q. In situ synthesis of porous ZnO-embedded Zn1-xCdxS/CdS heterostructures for enhanced photocatalytic activity. *CrystEngComm* **2016**, *18*, 1446–1452. [CrossRef]
166. Naterer, G.F.; Dincer, I.; Zamfirescu, C. Hybrid Copper–Chlorine Cycle. In *Hydrogen Production from Nuclear Energy*; Springer: London, UK, 2013; pp. 273–438. ISBN 9781447149385.
167. Wu, W.; Hsu, F.T.; Chen, H.Y. Design and energy evaluation of a stand-alone copper-chlorine (Cu-Cl) thermochemical cycle system for trigeneration of electricity, hydrogen, and oxygen. *Int. J. Energy Res.* **2018**, *42*, 830–842. [CrossRef]
168. Izanloo, M.; Mehrpooya, M. Investigation of a hybrid thermochemical Cu–Cl cycle, carbon capturing, and ammonia production process. *J. Therm. Anal. Calorim.* **2021**, *144*, 1907–1923. [CrossRef]

169. Osuolale, F.; Ogunleye, O.; Fakunle, M.; Busari, A.; Abolanle, Y. Comparative studies of Cu-Cl thermochemical water decomposition cyles for hydrogen production. *E3S Web Conf.* **2018**, *61*, 9. [CrossRef]
170. Razi, F.; Dincer, I.; Gabriel, K. Process Improvement and Analysis of an Integrated Four-Step Copper-Chlorine Cycle Modified with a Flash Vaporization Process for Hydrogen Production. *Energy and Fuels* **2021**, *35*, 9038–9046. [CrossRef]
171. Yilmaz, F.; Selbaş, R. Thermodynamic performance assessment of solar based Sulfur-Iodine thermochemical cycle for hydrogen generation. *Energy* **2017**, *140*, 520–529. [CrossRef]
172. Farsi, A.; Dincer, I.; Naterer, G.F. Review and evaluation of clean hydrogen production by the copper–chlorine thermochemical cycle. *J. Clean. Prod.* **2020**, *276*, 123833. [CrossRef]
173. Farsi, A.; Dincer, I.; Naterer, G.F. Exergo-economic assessment by a specific exergy costing method for an experimental thermochemical hydrogen production system. *Int. J. Energy Res.* **2021**, *45*, 17358–17377. [CrossRef]
174. Fan, G.; Ahmadi, A.; Ehyaei, M.A.; Das, B. Energy, exergy, economic and exergoenvironmental analyses of polygeneration system integrated gas cycle, absorption chiller, and Copper-Chlorine thermochemical cycle to produce power, cooling, and hydrogen. *Energy* **2021**, *222*, 120008. [CrossRef]
175. Naterer, G.F.; Suppiah, S.; Rosen, M.A.; Gabriel, K.; Dincer, I.; Jianu, O.A.; Wang, Z.; Easton, E.B.; Ikeda, B.M.; Rizvi, G.; et al. Advances in unit operations and materials for the Cu–Cl cycle of hydrogen production. *Int. J. Hydrogen Energy* **2017**, *42*, 15708–15723. [CrossRef]
176. Safari, F.; Dincer, I. A review and comparative evaluation of thermochemical water splitting cycles for hydrogen production. *Energy Convers. Manag.* **2020**, *205*, 112182. [CrossRef]
177. Diver, R.B.; Miller, J.E.; Allendorf, M.D.; Siegel, N.P.; Hogan, R.E. Solar thermochemical water-splitting ferrite-cycle heat engines. *J. Sol. Energy Eng. Trans. ASME* **2008**, *130*, 0410011–0410018. [CrossRef]
178. Bhosale, R.; Kumar, A.; AlMomani, F.; Ghosh, U.; Anis, M.S.; Kakosimos, K.; Shende, R.; Rosen, M.A. Solar hydrogen production via a samarium oxide-based thermochemical water splitting cycle. *Energies* **2016**, *9*, 316. [CrossRef]
179. Steinfeld, A. Solar hydrogen production via a two-step water-splitting thermochemical cycle based on Zn/ZnO redox reactions. *Int. J. Hydrogen Energy* **2002**, *27*, 611–619. [CrossRef]
180. Eidsvåg, H.; Bentouba, S.; Vajeeston, P.; Yohi, S.; Velauthapillai, D. Tio_2 as a photocatalyst for water splitting—an experimental and theoretical review. *Molecules* **2021**, *26*, 1687. [CrossRef] [PubMed]
181. Ni, M.; Leung, M.K.H.; Leung, D.Y.C.; Sumathy, K. A review and recent developments in photocatalytic water-splitting using TiO2 for hydrogen production. *Renew. Sustain. Energy Rev.* **2007**, *11*, 401–425. [CrossRef]
182. Zhang, Y.; Chen, J.; Xu, C.; Zhou, K.; Wang, Z.; Zhou, J.; Cen, K. A novel photo-thermochemical cycle of water-splitting for hydrogen production based on TiO_2-x/TiO_2. *Int. J. Hydrogen Energy* **2016**, *41*, 2215–2221. [CrossRef]
183. Zhou, Y.; Sun, Y.; Su, W.; Zhou, L. Experimental studies on the FeO/Fe_3O_4 cycle complemented with carbon gasification for producing hydrogen. *Energy and Fuels* **2013**, *27*, 4071–4076. [CrossRef]
184. Bhosale, R.R.; Kumar, A.; Van Den Broeke, L.J.P.; Gharbia, S.; Dardor, D.; Jilani, M.; Folady, J.; Al-Fakih, M.S.; Tarsad, M.A. Solar hydrogen production via thermochemical iron oxide-iron sulfate water splitting cycle. *Int. J. Hydrogen Energy* **2015**, *40*, 1639–1650. [CrossRef]
185. Bhosale, R.; Kumar, A.; Almomani, F. Solar Thermochemical Hydrogen Production via Terbium Oxide Based Redox Reactions. *Int. J. Photoenergy* **2016**, *2016*, 9727895. [CrossRef]
186. Marugán, J.; Botas, J.A.; Martín, M.; Molina, R.; Herradón, C. Study of the first step of the Mn2O3/MnO thermochemical cycle for solar hydrogen production. *Int. J. Hydrogen Energy* **2012**, *37*, 7017–7025. [CrossRef]
187. Bhosale, R.R.; Kumar, A.; AlMomani, F.; Ghosh, U.; Khraisheh, M. A comparative thermodynamic analysis of samarium and erbium oxide based solar thermochemical water splitting cycles. *Int. J. Hydrogen Energy* **2017**, *42*, 23416–23426. [CrossRef]
188. Charvin, P.; Abanades, S.; Flamant, G.; Lemort, F. Two-step water splitting thermochemical cycle based on iron oxide redox pair for solar hydrogen production. *Energy* **2007**, *32*, 1124–1133. [CrossRef]
189. D'Souza, L. Thermochemical hydrogen production from water using reducible oxide materials: A critical review. *Mater. Renew. Sustain. Energy* **2013**, *2*, 7. [CrossRef]
190. Mehrpooya, M.; Raeesi, M.; Pourfayaz, F.; Delpisheh, M. Investigation of a hybrid solar thermochemical water-splitting hydrogen production cycle and coal-fueled molten carbonate fuel cell power plant. *Sustain. Energy Technol. Assess.* **2021**, *47*, 101458. [CrossRef]
191. Kegel, J.; Povey, I.M.; Pemble, M.E. Zinc oxide for solar water splitting: A brief review of the material's challenges and associated opportunities. *Nano Energy* **2018**, *54*, 409–428. [CrossRef]
192. Haltiwanger, J.F.; Davidson, J.H.; Wilson, E.J. Renewable hydrogen from the Zn/ZnO solar thermochemical cycle: A cost and policy analysis. *J. Sol. Energy Eng. Trans. ASME* **2010**, *132*, 041011. [CrossRef]
193. Bhosale, R.R. Solar hydrogen production via ZnO/Zn based thermochemical water splitting cycle: Effect of partial reduction of ZnO. *Int. J. Hydrogen Energy* **2021**, *46*, 4739–4748. [CrossRef]
194. Loutzenhiser, P.G.; Meier, A.; Steinfeld, A. Review of the Two-Step H2O/CO2-Splitting solar thermochemical cycle based on Zn/ZnO redox reactions. *Materials* **2010**, *3*, 4922–4938. [CrossRef]
195. Fletcher, E.A. Solarthermal and solar quasi-electrolytic processing and separations: Zinc from zinc oxide as an example. *Ind. Eng. Chem. Res.* **1999**, *38*, 2275–2282. [CrossRef]

196. Müller, R.; Steinfeld, A. H2O-splitting thermochemical cycle based on ZnO/Zn-redox: Quenching the effluents from the ZnO dissociation. *Chem. Eng. Sci.* **2008**, *63*, 217–227. [CrossRef]
197. Wieckert, C.; Steinfeld, A. Solar thermal reduction of ZnO using CH4:ZnO and C:ZnO molar ratios less than 1. *J. Sol. Energy Eng. Trans. ASME* **2002**, *124*, 55–62. [CrossRef]
198. Bhosale, R.R. Thermodynamic efficiency analysis of ZnO/Zn based solar thermochemical CH_4 reforming and H_2O splitting cycle. *Int. J. Hydrogen Energy* **2020**, *45*, 5760–5771. [CrossRef]
199. Lindemer, M.D.; Advani, S.G.; Prasad, A.K. Experimental investigation of heterogeneous hydrolysis with Zn vapor under a temperature gradient. *Int. J. Hydrogen Energy* **2017**, *42*, 7847–7856. [CrossRef]
200. Gstoehl, D.; Brambilla, A.; Schunk, L.O.; Steinfeld, A. A quenching apparatus for the gaseous products of the solar thermal dissociation of ZnO. *J. Mater. Sci.* **2008**, *43*, 4729–4736. [CrossRef]
201. Alxneit, I. Assessing the feasibility of separating a stoichiometric mixture of zinc vapor and oxygen by a fast quench—Model calculations. *Sol. Energy* **2008**, *82*, 959–964. [CrossRef]
202. Lindemer, M.D.; Advani, S.G.; Prasad, A.K. Hydrogen production via the heterogeneous hydrolysis of Zn vapor under a temperature gradient: Modeling and efficiency analysis. *Int. J. Hydrogen Energy* **2016**, *41*, 10557–10567. [CrossRef]
203. Xiao, L.; Wu, S.Y.; Li, Y.R. Advances in solar hydrogen production via two-step water-splitting thermochemical cycles based on metal redox reactions. *Renew. Energy* **2012**, *41*, 1–12. [CrossRef]
204. Koepf, E.; Villasmil, W.; Meier, A. Pilot-scale solar reactor operation and characterization for fuel production via the Zn/ZnO thermochemical cycle. *Appl. Energy* **2016**, *165*, 1004–1023. [CrossRef]
205. Abanades, S.; Charvin, P.; Lemont, F.; Flamant, G. Novel two-step SnO_2/SnO water-splitting cycle for solar thermochemical production of hydrogen. *Int. J. Hydrogen Energy* **2008**, *33*, 6021–6030. [CrossRef]
206. Charvin, P.; Abanades, S.; Lemont, F.; Flamant, G. Experimental Study of SnO2/SnO/Sn Thermochemical Systems for Solar Production of Hydrogen. *AIChE J.* **2008**, *54*, 2759–2767. [CrossRef]
207. Chambon, M.; Abanades, S.; Flamant, G. Solar thermal reduction of ZnO and SnO_2: Characterization of the recombination reaction with O2. *Chem. Eng. Sci.* **2010**, *65*, 3671–3680. [CrossRef]
208. Levêque, G.; Abanades, S.; Jumas, J.C.; Olivier-Fourcade, J. Characterization of two-step tin-based redox system for thermochemical fuel production from solar-driven CO_2 and H_2O splitting cycle. *Ind. Eng. Chem. Res.* **2014**, *53*, 5668–5677. [CrossRef]
209. Bhosale, R.R.; Kumar, A.; Sutar, P. Thermodynamic analysis of solar driven SnO2/SnO based thermochemical water splitting cycle. *Energy Convers. Manag.* **2017**, *135*, 226–235. [CrossRef]
210. Mao, Y.; Gao, Y.; Dong, W.; Wu, H.; Song, Z.; Zhao, X.; Sun, J.; Wang, W. Hydrogen production via a two-step water splitting thermochemical cycle based on metal oxide—A review. *Appl. Energy* **2020**, *267*, 114860. [CrossRef]
211. Chambon, M.; Abanades, S.; Flamant, G. Kinetic investigation of hydrogen generation from hydrolysis of SnO and Zn solar nanopowders. *Int. J. Hydrogen Energy* **2009**, *34*, 5326–5336. [CrossRef]
212. Vishnevetsky, I.; Epstein, M. Tin as a possible candidate for solar thermochemical redox process for hydrogen production. *J. Sol. Energy Eng. Trans. ASME* **2009**, *131*, 0210071–0210078. [CrossRef]
213. Nakumura, T. Hydrogen Production From Water Utilizing. *Sol. Energy* **1977**, *19*, 467–475. [CrossRef]
214. Kodama, T.; Gokon, N.; Yamamoto, R. Thermochemical two-step water splitting by ZrO_2-supported $NixFe_3$-xO_4 for solar hydrogen production. *Sol. Energy* **2008**, *82*, 73–79. [CrossRef]
215. Charvin, P.; Stéphane, A.; Florent, L.; Gilles, F. Analysis of solar chemical processes for hydrogen production from water splitting thermochemical cycles. *Energy Convers. Manag.* **2008**, *49*, 1547–1556. [CrossRef]
216. Xu, R.; Wiesner, T.F. Conceptual design of a two-step solar hydrogen thermochemical cycle with thermal storage in a reaction intermediate. *Int. J. Hydrogen Energy* **2014**, *39*, 12457–12471. [CrossRef]
217. Goikoetxea, N.B.; Gómez-Mancebo, M.B.; Fernández-Saavedra, R.; Borlaf, F.; García-Pérez, F.; Jiménez, J.A.; Llorente, I.; Rucandio, I.; Quejido, A.J. Understanding water-splitting thermochemical cycles based on nickel and cobalt ferrites for hydrogen production. *Int. J. Hydrogen Energy* **2019**, *44*, 17578–17585. [CrossRef]
218. Teknetzi, I.; Nessi, P.; Zaspalis, V.; Nalbandian, L. Ni-ferrite with structural stability for solar thermochemical H_2O/CO_2 splitting. *Int. J. Hydrogen Energy* **2017**, *42*, 26231–26242. [CrossRef]
219. Amar, V.S.; Puszynski, J.A.; Shende, R.V. H2 generation from thermochemical water-splitting using yttria stabilized NiFe2O4 core-shell nanoparticles. *J. Renew. Sustain. Energy* **2015**, *7*, 023113. [CrossRef]
220. Gokon, N.; Murayama, H.; Umeda, J.; Hatamachi, T.; Kodama, T. Monoclinic zirconia-supported Fe_3O_4 for the two-step water-splitting thermochemical cycle at high thermal reduction temperatures of 1400–1600 °C. *Int. J. Hydrogen Energy* **2009**, *34*, 1208–1217. [CrossRef]
221. Kodama, T.; Kondoh, Y.; Yamamoto, R.; Andou, H.; Satou, N. Thermochemical hydrogen production by a redox system of ZrO_2-supported Co(II)-ferrite. *Sol. Energy* **2005**, *78*, 623–631. [CrossRef]
222. Reñones, P.; Alvarez-Galvan, M.C.; Ruiz-Matas, L.; Retuerto, M.; Navarro, R.M.; Fierro, J.L.G. Nickel ferrite supported on calcium-stabilized zirconia for solar hydrogen production by two-step thermochemical water splitting. *Mater. Today Energy* **2017**, *6*, 248–254. [CrossRef]
223. Fernández-Saavedra, R.; Gómez-Mancebo, M.B.; Caravaca, C.; Sánchez, M.; Quejido, A.J.; Vidal, A. Hydrogen production by two-step thermochemical cycles based on commercial nickel ferrite: Kinetic and structural study. *Int. J. Hydrogen Energy* **2014**, *39*, 6819–6826. [CrossRef]

224. Scheffe, J.R.; Li, J.; Weimer, A.W. A spinel ferrite/hercynite water-splitting redox cycle. *Int. J. Hydrogen Energy* **2010**, *35*, 3333–3340. [CrossRef]
225. Kreider, P.B.; Funke, H.H.; Cuche, K.; Schmidt, M.; Steinfeld, A.; Weimer, A.W. Manganese oxide based thermochemical hydrogen production cycle. *Int. J. Hydrogen Energy* **2011**, *36*, 7028–7037. [CrossRef]
226. Marugán, J.; Botas, J.A.; Molina, R.; Herradón, C. Study of the hydrogen production step of the Mn_2O_3/MnO thermochemical cycle. *Int. J. Hydrogen Energy* **2014**, *39*, 5274–5282. [CrossRef]
227. Abou-El-Sherbini, K.S.; Askar, M.H.; Schöllhorn, R. Hydrated layered manganese dioxide: Part I. Synthesis and characterization of some hydrated layered manganese dioxides from α-$NaMnO_2$. *Solid State Ionics* **2002**, *150*, 407–415. [CrossRef]
228. Omomo, Y.; Sasaki, T.; Watanabe, M. Preparation of protonic layered manganates and their intercalation behavior. *Solid State Ionics* **2002**, *151*, 243–250. [CrossRef]
229. Rao, C.N.R.; Dey, S. Solar thermochemical splitting of water to generate hydrogen. *Proc. Natl. Acad. Sci. USA* **2017**, *114*, 13385–13393. [CrossRef] [PubMed]
230. Francis, T.M.; Lichty, P.R.; Weimer, A.W. Manganese oxide dissociation kinetics for the Mn2O3 thermochemical water-splitting cycle. Part 1: Experimental. *Chem. Eng. Sci.* **2010**, *65*, 3709–3717. [CrossRef]
231. Bayón, A.; De La Peña O'Shea, V.A.; Serrano, D.P.; Coronado, J.M. Influence of structural and morphological characteristics on the hydrogen production and sodium recovery in the NaOH-MnO thermochemical cycle. *Int. J. Hydrogen Energy* **2013**, *38*, 13143–13152. [CrossRef]
232. Orfila, M.; Linares, M.; Molina, R.; Marugán, J.; Botas, J.Á.; Sanz, R. Hydrogen production by water splitting with Mn3-x$CoxO_4$ mixed oxides thermochemical cycles: A thermodynamic analysis. *Energy Convers. Manag.* **2020**, *216*, 112945. [CrossRef]
233. Xu, B.; Bhawe, Y.; Davis, M.E. Low-temperature, manganese oxide-based, thermochemical water splitting cycle. *Proc. Natl. Acad. Sci. USA* **2012**, *109*, 9260–9264. [CrossRef]
234. Bayón, A.; De La Penã O'Shea, V.A.; Serrano, D.P.; Coronado, J.M. Exploring the alternative MnO-Na_2CO_3 thermochemical cycle for water splitting. *J. CO_2 Util.* **2020**, *42*, 101264. [CrossRef]
235. Bayón, A.; De La Peña O'Shea, V.A.; Coronado, J.M.; Serrano, D.P. Role of the physicochemical properties of hausmannite on the hydrogen production via the Mn3O4-NaOH thermochemical cycle. *Int. J. Hydrogen Energy* **2016**, *41*, 113–122. [CrossRef]
236. Murmura, M.A.; Varsano, F.; Padella, F.; La Barbera, A.; Alvani, C.; Annesini, M.C. Hydrogen production by the sodium manganese ferrite thermochemical cycle-experimental rate and modeling. *Ind. Eng. Chem. Res.* **2014**, *53*, 10310–10317. [CrossRef]
237. Orfila, M.; Sanz, D.; Linares, M.; Molina, R.; Sanz, R.; Marugán, J.; Botas, J.Á. H_2 production by thermochemical water splitting with reticulated porous structures of ceria-based mixed oxide materials. *Int. J. Hydrogen Energy* **2021**, *46*, 17458–17471. [CrossRef]
238. Abanades, S.; Legal, A.; Cordier, A.; Peraudeau, G.; Flamant, G.; Julbe, A. Investigation of reactive cerium-based oxides for H2 production by thermochemical two-step water-splitting. *J. Mater. Sci.* **2010**, *45*, 4163–4173. [CrossRef]
239. Vedyagin, A.A.; Karnaukhov, T.M.; Cherepanova, S.V.; Stoyanovskii, V.O.; Rogov, V.A.; Mishakov, I.V. Synthesis of binary Co–Mg–O oxide system and study of its behavior in reduction/oxidation cycling. *Int. J. Hydrogen Energy* **2019**, *44*, 20690–20699. [CrossRef]
240. Karnaukhov, T.M.; Vedyagin, A.A.; Cherepanova, S.V.; Rogov, V.A.; Mishakov, I.V. Sol–gel synthesis and characterization of the binary Ni–Mg–O oxide system. *J. Sol-Gel Sci. Technol.* **2019**, *92*, 208–214. [CrossRef]
241. Muhich, C.L.; Ehrhart, B.D.; Al-shankiti, I.; Ward, B.J.; Musgrave, C.B.; Weimer, A.W. A review and perspective of efficient hydrogen generation via solar thermal water splitting. *Wiley Interdiscip. Rev. Energy Environ.* **2016**, *5*, 261–287. [CrossRef]
242. Orfila, M.; Linares, M.; Molina, R.; Botas, J.Á.; Marugán, J.; Sanz, R. Thermochemical hydrogen production using manganese cobalt spinels as redox materials. *Int. J. Hydrogen Energy* **2017**, *42*, 13532–13543. [CrossRef]
243. Miller, J.E.; Allendorf, M.D.; Diver, R.B.; Evans, L.R.; Siegel, N.P.; Stuecker, J.N. Metal oxide composites and structures for ultra-high temperature solar thermochemical cycles. *J. Mater. Sci.* **2008**, *43*, 4714–4728. [CrossRef]
244. Kodama, T.; Gokon, N. Thermochemical cycles for high-temperature solar hydrogen production. *Chem. Rev.* **2007**, *107*, 4048–4077. [CrossRef]
245. Chen, Z.; Jiang, Q.; Tong, J.; Yang, M.; Jiang, Z.; Li, C. Influences of morphology and structure on Mn-based multi-step thermochemical H_2O splitting cycle. *Sol. Energy* **2016**, *129*, 236–243. [CrossRef]
246. Ishaq, H.; Dincer, I. A comparative evaluation of three Cu-Cl cycles for hydrogen production. *Int. J. Hydrogen Energy* **2019**, *44*, 7958–7968. [CrossRef]
247. Murmura, M.A.; Vilardi, G. Energy and exergy analysis of the zinc/zinc oxide thermochemical cycle for hydrogen production and fuel cell power generation. *Energy Convers. Manag.* **2021**, *247*, 114761. [CrossRef]
248. Wang, Y.; Sharma, A.; Duong, T.; Arandiyan, H.; Zhao, T.; Zhang, D.; Su, Z.; Garbrecht, M.; Beck, F.J.; Karuturi, S.; et al. Direct Solar Hydrogen Generation at 20% Efficiency Using Low-Cost Materials. *Adv. Energy Mater.* **2021**, *11*, 2101053. [CrossRef]
249. Jia, J.; Seitz, L.C.; Benck, J.D.; Huo, Y.; Chen, Y.; Ng, J.W.D.; Bilir, T.; Harris, J.S.; Jaramillo, T.F. Solar water splitting by photovoltaic-electrolysis with a solar-to-hydrogen efficiency over 30%. *Nat. Commun.* **2016**, *7*, 13237. [CrossRef] [PubMed]
250. Gorensek, M.; Summers, W.; Boltrunis, C.; Lahoda, E.; Allen, D.; Greyvenstein, R. *Hybrid Sulfur Process Reference Design and Cost Analysis*; Report No. SRNL-L1200-2008-00002; Savannah River National Laboratory: Jackson, SC, USA, 2009.
251. Kromer, M.; Roth, K.; Takata, R.; Chin, P. *Support for Cost Analyses on Solar-Driven High Temperature Thermochemical Water-Splitting Cycles*; Final Report to Department of Energy, Order DE-DT0000951; TIAX LLC: Lexington, MA, USA, 2011.
252. *U.S. Department of Energy HydroGEN Program*.

253. Leybros, J.; Gilardi, T.; Saturnin, A.; Mansilla, C.; Carles, P. Plant sizing and evaluation of hydrogen production costs from advanced processes coupled to a nuclear heat source. Part I: Sulphur-iodine cycle. *Int. J. Hydrogen Energy* **2010**, *35*, 1008–1018. [CrossRef]
254. Le Duigou, A.; Borgard, J.M.; Larousse, B.; Doizi, D.; Allen, R.; Ewan, B.C.; Priestman, G.H.; Elder, R.; Devonshire, R.; Ramos, V.; et al. HYTHEC: An EC funded search for a long term massive hydrogen production route using solar and nuclear technologies. *Int. J. Hydrogen Energy* **2007**, *32*, 1516–1529. [CrossRef]